



**RESEARCH ARTICLE**

# Outer hair cell electromotility is low-pass filtered relative to the molecular conformational changes that produce nonlinear capacitance

 Joseph Santos-Sacchi<sup>1,2,3</sup> , Kuni H. Iwasa<sup>4</sup> , and Winston Tan<sup>1</sup> 

The outer hair cell (OHC) of the organ of Corti underlies a process that enhances hearing, termed cochlear amplification. The cell possesses a unique voltage-sensing protein, prestin, that changes conformation to cause cell length changes, a process termed electromotility (eM). The prestin voltage sensor generates a capacitance that is both voltage- and frequency-dependent, peaking at a characteristic membrane voltage ( $V_h$ ), which can be greater than the linear capacitance of the OHC. Accordingly, the OHC membrane time constant depends upon resting potential and the frequency of AC stimulation. The confounding influence of this multifarious time constant on eM frequency response has never been addressed. After correcting for this influence on the whole-cell voltage clamp time constant, we find that both guinea pig and mouse OHC eM is low pass, substantially attenuating in magnitude within the frequency bandwidth of human speech. The frequency response is slowest at  $V_h$ , with a cut-off, approximated by single Lorentzian fits within that bandwidth, near 1.5 kHz for the guinea pig OHC and near 4.3 kHz for the mouse OHC, each increasing in a U-shaped manner as holding voltage deviates from  $V_h$ . Nonlinear capacitance (NLC) measurements follow this pattern, with cut-offs about double that for eM. Macro-patch experiments on OHC lateral membranes, where voltage delivery has high fidelity, confirms low pass roll-off for NLC. The U-shaped voltage dependence of the eM roll-off frequency is consistent with prestin's voltage-dependent transition rates. Modeling indicates that the disparity in frequency cut-offs between eM and NLC may be attributed to viscoelastic coupling between prestin's molecular conformations and nanoscale movements of the cell, possibly via the cytoskeleton, indicating that eM is limited by the OHC's internal environment, as well as the external environment. Our data suggest that the influence of OHC eM on cochlear amplification at higher frequencies needs reassessment.

## Introduction

Outer hair cell (OHC) electromotility (eM) underlies cochlear amplification in mammals, where in its absence, hearing deficits amount to 40–60 dB (Dallos et al., 2008; Ashmore et al., 2010). The molecular basis of OHC eM is the membrane-bound protein prestin (SLC26a5), an anion transporter family member that has evolved to work as a voltage-dependent motor protein in these cells (Zheng et al., 2000). The protein's voltage-sensor activity presents as a voltage-dependent (or nonlinear) capacitance (NLC), obeying Boltzmann statistics (Ashmore, 1990; Santos-Sacchi, 1991), and whose peak magnitude corresponds to the voltage ( $V_h$ ) where sensor charge is equally displaced to either side of the membrane. Voltage-dependent conformational change in prestin is believed to form the basis of precise phase differences between OHC activity and basilar membrane motion

that leads to amplification, indicative of local cycle-by-cycle feedback (Dallos et al., 2008). Recent measurements of OHC extracellular voltage and basilar membrane motion have observed the predicted amplifying phase differences (Dong and Olson, 2013). However, other recent measurements did not find appropriate phase or timing differences in the motions within the organ of Corti, and have challenged the standard view of amplification (Ren et al., 2016; He et al., 2018). Additionally, it is commonly accepted that unconstrained (load-free) OHC eM magnitude is invariant across stimulating frequency, having been measured out beyond 70 kHz (Frank et al., 1999); the flat frequency response is another important element in cycle-by-cycle feedback theory. However, these data were obtained at voltage offsets far removed from  $V_h$ , which has questionable

<sup>1</sup>Department of Surgery (Otolaryngology), Yale University School of Medicine, New Haven, CT; <sup>2</sup>Department of Neuroscience, Yale University School of Medicine, New Haven, CT; <sup>3</sup>Department of Cellular and Molecular Physiology, Yale University School of Medicine, New Haven, CT; <sup>4</sup>National Institute on Deafness and Other Communication Disorders, National Institutes of Health, Bethesda, MD.

Correspondence to Joseph Santos-Sacchi: [joseph.santos-sacchi@yale.edu](mailto:joseph.santos-sacchi@yale.edu).

© 2019 Santos-Sacchi et al. This article is distributed under the terms of an Attribution–Noncommercial–Share Alike–No Mirror Sites license for the first six months after the publication date (see <http://www.rupress.org/terms/>). After six months it is available under a Creative Commons License (Attribution–Noncommercial–Share Alike 4.0 International license, as described at <https://creativecommons.org/licenses/by-nc-sa/4.0/>).

physiological significance. Based on our measures (Santos-Sacchi and Tan, 2018), we estimate that their depolarized offset from  $V_h$  would have been  $\sim 65$  mV. Indeed, by exploring at an offset potential near  $V_h$ , we recently demonstrated that eM measured with the microchamber displays significant low-pass behavior (Santos-Sacchi and Tan, 2018). Here we further explore the low-pass nature of eM under whole-cell voltage clamp out to 6.25 kHz in the guinea pig and mouse with ramped changes in holding potential that provide shorter, more stationary-in-time measures compared with our previous experiments. Furthermore, whole-cell voltage clamp provides far better voltage control than the microchamber, but patch electrode series resistance effects must be considered. Following precise corrections for NLC-induced, voltage- and frequency-dependent voltage roll-off under whole-cell voltage clamp, never previously done, we find that eM and NLC show similarities in their nonlinear voltage and frequency dependence, both frequency cut-offs being U-shaped functions of holding voltage, with minima near  $V_h$ . Macro-patch experiments on the OHC lateral membrane, which provide robust voltage control, confirm our low-pass whole-cell measures of NLC within the speech frequency range. We further find that the frequency cut-offs of eM and NLC are disparate. Modeling suggests that both internal (e.g., cytoskeletal interactions, membrane lipid interactions) and external (e.g., viscous environment of the cell) loads are influential in effecting this disparity.

## Materials and methods

Whole-cell recordings were made from single isolated OHCs from the apical two turns of organ of Corti of guinea pigs. An inverted Nikon Eclipse TI-2000 microscope with a 40 $\times$  lens was used to observe cells during voltage clamp. Experiments were performed at room temperature. Blocking solutions were used to remove ionic currents, limiting confounding effects on NLC determination and voltage delivery under voltage clamp (Santos-Sacchi, 1991; Santos-Sacchi and Song, 2016). Extracellular solution was (in mM): NaCl 100, TEA-Cl 20, CsCl 20, CoCl<sub>2</sub> 2, MgCl<sub>2</sub> 1, CaCl<sub>2</sub> 1, and HEPES 10. Intracellular solution was (in mM): CsCl 140, MgCl<sub>2</sub> 2, HEPES 10, and EGTA 10. All chemicals were purchased from Sigma-Aldrich.

An Axon 200B amplifier was used for whole-cell recording with jClamp software (<http://www.scisoftco.com>). An Axon Digidata 1440 was used for digitizing. AC (frequency) analysis of membrane currents ( $I_m$ ) and eM were made by stimulating cells with a voltage ramp from 100 to  $-110$  mV (nominal), superimposed with summed AC voltages at harmonically related frequencies of 195.3, 390.6, 781.3, 1,562.5, 3,125, and 6,250 Hz, with a 10- $\mu$ s sample clock. Currents were filtered at 10 kHz with a four-pole Bessel filter. Corrections for series resistance were made during analysis. Capacitance was measured using dual-sine analysis at harmonic frequencies (Santos-Sacchi et al., 1998; Santos-Sacchi, 2004). Briefly, real and imaginary components of membrane current at harmonic frequencies were determined by Fast Fourier Transform (FFT) in jClamp, corrected for the roll-off of recording system admittance (Gillis, 1995) and stray capacitance (Santos-Sacchi, 2018). Series resistance ( $R_s$ ),

membrane resistance ( $R_m$ ), and membrane capacitance ( $C_m$ ) were extracted using the dual-sine, three-parameter solution of the standard patch clamp model (Santos-Sacchi et al., 1998; Santos-Sacchi, 2004), based on the original single sine solution (Pusch and Neher, 1988). To extract Boltzmann parameters, capacitance-voltage data were fit to the first derivative of a two-state Boltzmann function.

$$C_m = NLC + C_{lin} = Q_{max} \frac{ze}{k_B T} \frac{b}{(1+b)^2} + C_{lin}, \quad (1)$$

where

$$b = \exp\left(-ze \frac{V_m - V_h}{k_B T}\right).$$

$Q_{max}$  is the maximum nonlinear charge moved,  $V_h$  is voltage at peak capacitance or equivalently, at half-maximum charge transfer,  $V_m$  is membrane potential,  $z$  is valence,  $C_{lin}$  is linear membrane capacitance,  $e$  is electron charge,  $k_B$  is Boltzmann's constant, and  $T$  is absolute temperature.

As noted above, whole-cell NLC determination was made following stray capacitance removal (Santos-Sacchi et al., 1998; Santos-Sacchi and Song, 2016; Santos-Sacchi, 2018; Santos-Sacchi and Tan, 2018). Patch pipettes were coated with M-coat (Micro Measurements) to reduce stray capacitance. Remaining stray capacitance was removed by amplifier compensation circuitry before establishing whole-cell configuration, and if necessary, additional compensation was applied under whole-cell voltage-clamp conditions (Schnee et al., 2011a,b) and/or through a software algorithm within jClamp software to ensure expected frequency-independent linear capacitance (Santos-Sacchi and Song, 2016; Santos-Sacchi, 2018). The latter approach simply performs single tau capacitance compensation mathematically on collected data, analogous to the electronic compensation with the amplifier.  $R_s$  was determined from voltage step-induced whole-cell currents before AC measures, the derivation provided in the appendix of (Huang and Santos-Sacchi, 1993).  $R_m(v)$  across ramp voltage was determined from  $R_s$ -corrected ramp voltage and generated ramp currents with AC components removed,  $\Delta V_m / (\Delta I_{R_s})$ .

Simultaneous and synchronous eM measures were made with fast video recording. A Phantom 110 or 310 camera (Vision Research) was used for video measures at a frame rate of 25 kHz. Magnification was set to provide 176 or 106 nm/pixel. A method was developed to track the apical image of the OHC, providing subpixel resolution of movements (see Fig. 1). Video frames were filtered with a Gaussian Blur filter (<http://www.gimp.org>) before measurement. The patch electrode provided a fixed point near the basal end of the cell. Since movements were measured at the apical pole of the cell and the cell was held physically at the point of electrode insertion, estimates of full whole-cell movements were obtained from the ratio of apical/basal partitioning at the point of electrode insertion as in microchamber experiments (Frank et al., 1999; Santos-Sacchi and Tan, 2018). Resultant movements were analyzed by FFT in MATLAB. The colors in surface plots were generated in the MATLAB plotting routine *surf* with shading set to <interp>. This procedure allows contours to be readily observable. Although eM was measured at all

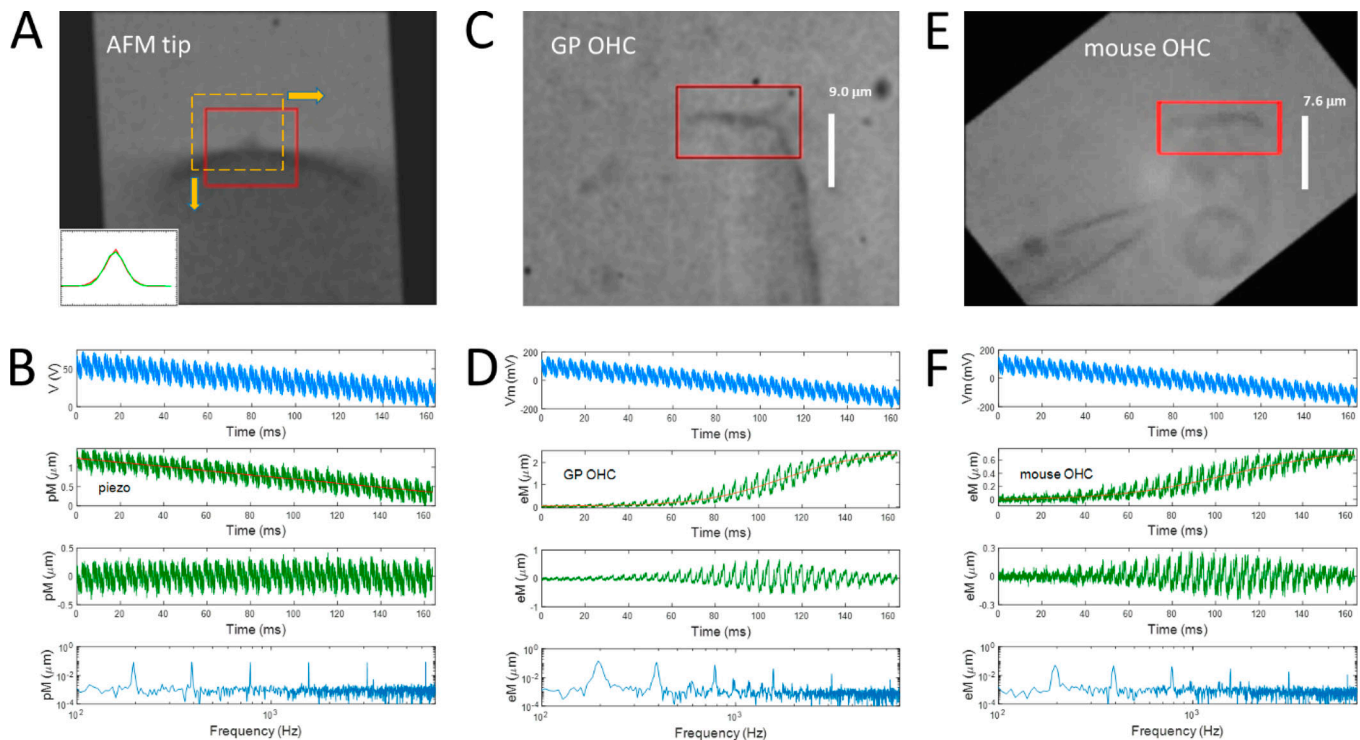


Figure 1. **Motion measures from fast video using a shape tracking algorithm implemented in the program jClamp.** (A) Frame of an AFM probe tip with a fiducial red box delimiting a region of the image to track. For each frame in the video stream, the image was sampled at single pixel offsets of  $\pm 10$  pixels in both the vertical and horizontal dimensions (yellow dotted box) relative to the fiducial image. Rotation of the image was possible to maximize displacements to a single dimension. A pixel comparison was made (subtraction of sampled image pixels from fiducial pixels and summed). The resulting distribution along the x and y axis was fit with a Gaussian function to obtain subpixel image movements. (B) Panel 1 shows the voltage command to the piezo stack. Panel 2 shows the piezo movements (pM) induced by the voltage command. The red line is a linear fit used to detrend the data (Panel 3), before FFT of the whole duration response (Panel 4). The magnitude plot shows high fidelity in capturing tip movements across frequency. (C) The apical portion of a guinea pig OHC under whole-cell voltage clamp was similarly tracked. (D) Panel 1 shows voltage clamp command. Panel 2 shows OHC eM. The red line is a sigmoidal fit used to detrend the data (Panel 3), before FFT of the whole duration response (Panel 4). (E and F) Similar results for a mouse OHC. Unlike the piezo response, eM falls precipitously across frequency. The frequency response arises from  $\tau_{\text{clamp}}$  and the intrinsic low-pass nature of eM. The removal of  $\tau_{\text{clamp}}$  contribution is easily accomplished (see Results). GP, guinea pig.

six AC frequencies, only five estimates of NLC were possible using the dual-sine approach. To obtain  $\tau_{\text{clamp}}$  estimates at 6.25 kHz, the magnitude of NLC at 3.125 kHz was used, factored by 0.748, in line with the slope of its decrease across frequency.

Models were implemented in MATLAB Simulink and Simscape, as detailed previously (Song and Santos-Sacchi, 2013; Santos-Sacchi and Song, 2014b). Model  $R_s$  and  $R_m$  were from the averages of guinea pig and mouse OHC parameters obtained (see below).  $R_s$ -corrected  $V_m$  vs. eM data were fit with the first derivative of a two-state Boltzmann function (Santos-Sacchi, 1991). We processed biophysical data as either group-averaged (whole-cell currents and eM averaged before analysis) or individual cell analysis followed by averaging, thus providing statistics (mean  $\pm$  SEM).

Under voltage clamp, the voltage delivered across the cell membrane depends on the electrode  $R_s$ . In the absence of  $R_s$ , the command voltage is delivered faithfully to the cell membrane in magnitude and time (phase). Otherwise, the voltage delivered to the membrane will suffer from voltage drops across  $R_s$ , depending on the magnitude and time (phase) of evoked currents. In any analysis of voltage-dependent cellular processes, such as eM (Santos-Sacchi and Dilger, 1988; Iwasa and Kachar, 1989), it

is important to accurately assess membrane voltage. Actual membrane potential under voltage clamp can be exactly determined by subtraction of the voltage drop across  $R_s$ , i.e.,  $I_{R_s} * R_s$ , with  $I_{R_s}$  being the sum of resistive and capacitive components of the cell membrane current. For sinusoidal stimulation across the voltage ramp, the AC command voltage  $V_c$  and evoked currents  $I_{R_s}$  are evaluated as complex values at each excitation frequency and ramp offset voltage,  $(A + jB)$ , where A and B are the real and imaginary components, obtained by FFT, thereby supplying  $V_c(f, v)$  and  $I_{R_s}(f, v)$ . Our goal is to accurately determine the frequency response of eM, given a nonzero series resistance that imposes its own influence on the frequency response of voltage-driven eM data. The method essentially seeks to identify the true excitation voltage,  $V_m(f, v)$ , i.e., the drive for eM, supplied to the plasma membrane.

Before we present an analysis of averaged eM data, we illustrate the approaches available for  $R_s$  correction in a MATLAB Simulink model. In the model, we are able to directly measure imposed membrane voltage so we can compare results from these approaches to actual values. The generated charge in the model is taken as the equivalent of eM, since we have shown that OHC eM and prestin charge movement are

directly coupled (Santos-Sacchi and Tan, 2018). The model we use to confirm our voltage corrections has been fully described before (Santos-Sacchi and Song, 2014a), and includes a slow, stretched exponential intermediary transition between chloride binding transitions and voltage-dependent charge transitions, the latter corresponding to eM. Modifications of the model were made to correspond to the biophysical data. Chloride was 140 mM. For the model, the number of prestin particles was set to 25.92e6, and  $z = 0.92$  for the guinea pig, and correspondingly 5.62e6, and 1 for the mouse. The forward ( $\alpha$ ) and backward ( $\beta$ ) voltage-dependent transition rate constants for the electromechanical component of the model were 1.2947e6 and 1.1558e4, respectively. Both forward ( $\alpha_m$ ) and backward ( $\beta_m$ ) parallel intermediary transition rate constants (which are equal to each other, but separately labeled to distinguish direction—incidentally, the equivalence is the basis of detailed balance in the model) were defined as

$$\alpha_m, \beta_m = A \cdot \exp(b \cdot m), \text{ for } m = 0.. 26, \quad (2)$$

where  $b = -0.4663$  and  $A = 3.0398e4$  for the guinea pig data comparisons, or  $A = 15.199$  for the mouse data comparisons to account for the difference in NLC and eM frequency response of the species that we find. Units for rate constants and  $A$  are in  $s^{-1}$ ;  $b$  is unitless.

For the model, there are three ways to correct the frequency response of eM magnitude for the confounding effects of  $R_s$ -induced membrane voltage roll-off.

### Method 1

The complex ratio of AC command voltage (located at differing ramp voltage offsets [ $v$ ]) to the directly measured membrane voltage within the model at each excitation frequency can be used to correct eM magnitude frequency response, eM being both a function of frequency and holding voltage (Santos-Sacchi and Tan, 2018), namely, eM ( $f, v$ ), akin to NLC ( $f, v$ ) (Santos-Sacchi and Song, 2016). Parallel bars indicate absolute values:

$$V_m(f, v) = V_m(f, v)_{\text{model}} \quad (3)$$

$$|eM(f, v)_{\text{actual}}| = \left| eM(f, v)_{\text{measured}} \cdot \frac{V_c(f, v)}{V_m(f, v)} \right| \quad (4)$$

### Method 2

The complex ratio of command voltage to calculated  $V_m(f, v)$ , namely,  $I_{R_s}(f, v) \cdot R_s$ , can be used for correction.

$$V_m(f, v) = V_c(f, v) - I_{R_s}(f, v) \cdot R_s \quad (5)$$

$$|eM(f, v)_{\text{actual}}| = \left| eM(f, v)_{\text{measured}} \cdot \frac{V_c(f, v)}{V_m(f, v)} \right| \quad (6)$$

### Method 3

Finally, the multifarious clamp time constant,  $\tau_{\text{clamp}}(f, v)$ , determined at each excitation frequency and ramp voltage offset, can be used to correct, via a Lorentzian function ( $A=1/[1+(2\pi f\tau)^2]^{1/2}$ ), the magnitude of eM, scaled to DC (steady state) levels  $[1 - R_s/R_m(f_0, v)]$ ,  $f_0 = 0 \approx$  ramp frequency.

$$\tau_{\text{clamp}}(f, v) = [C_{\text{lin}} + \text{NLC}(f, v)] \cdot R_{\parallel}(f_0, v), \quad (7)$$

where

$$R_{\parallel}(f_0, v) = \frac{R_s \cdot R_m(f_0, v)}{R_s + R_m(f_0, v)} \quad (8)$$

$$V_m(f, v) = V_c(f, v) \cdot \frac{[1 - \frac{R_s}{R_m(f_0, v)}]}{[1 + (2\pi f \cdot \tau_{\text{clamp}}(f, v))^2]^{1/2}} \quad (9)$$

$$|eM(f, v)_{\text{actual}}| = \left| eM(f, v)_{\text{measured}} \cdot \frac{V_c(f, v)}{V_m(f, v)} \right| \quad (9)$$

For the model, Fig. S1 (guinea pig parameters) and Fig. S2 (mouse parameters) show that each method of  $R_s$  correction gives the same results, revealing the intrinsic low pass eM response of the meno presto model that derives from its stretched-exponential intermediary transition kinetics (Song and Santos-Sacchi, 2013; Santos-Sacchi and Tan, 2018).

Because  $R_s$  was measured before running the ramp protocols, there is always a possibility that it changed during recording. The possibility of slight changes in  $R_s$  is well established in the literature. Fortunately, the currents generated simultaneously with eM must also report on  $R_s$ . Thus, we plot frequency cut-offs of eM based on Methods 2 and 3, each showing overlap (see Fig. 6), and indicating that our estimates of  $R_s$  are indeed accurate, with only minor corrections of the initial estimates ( $0.95\text{--}1.05 \times$  initial estimates).

For the on-cell macro-patch approach, we used pipette inner diameters of  $3.31 \pm 0.24 \mu\text{m}$  (electrode resistance in bath  $1.49 \pm 0.04 \text{ M}\Omega$ ,  $n = 10$ ), with M-coat applied within  $\sim 20 \mu\text{m}$  of the tip. Extracellular solution was in the pipette. To establish Gohm seals ( $2.7 \pm 0.24 \text{ G}\Omega$ ,  $n = 10$ ) we supplemented extracellular solution with  $5\text{--}7.5 \mu\text{M Gd}^{+3}$ ; we have shown previously that these low concentrations help to form seals without affecting NLC (Santos-Sacchi and Song, 2016). Ramps with superimposed sinusoids were used, as above. Subtraction of currents at very depolarized potentials, where predominantly linear membrane capacitance and stray capacitance contribute, provided prestin-associated nonlinear currents (see Fig. 7). Subsequently, these nonlinear capacitive currents were used for dual-sine capacitance estimation.

Data points from previous publications were extracted from plots using the application Grabit (written by Jiro Doke) in MATLAB.

### Online supplemental material

Figs. S1 and S2 depict model data of the meno presto model for guinea pig and mouse. Each illustrates that voltage corrections used on the collected cell data are accurate and appropriate.

## Results

Fig. 1 depicts the method used to measure eM. Movement of a piezo-driven AFM tip ( $0.2 \text{ N/m}$ ) confirmed the fidelity of the measuring technique out to  $6,250 \text{ Hz}$  (Fig. 1 B, panel 4). To obtain accurate FFT results, the ramp-induced movement was detrended by subtracting a linear fit for the AFM tip measures or a sigmoidal fit for the guinea pig or mouse OHC eM measures (Fig. 1, B panel 3; D, panel 3; and F, panel 3). Subsequent analyses followed this detrending approach. In Fig. 1, D and F, panel 4, an

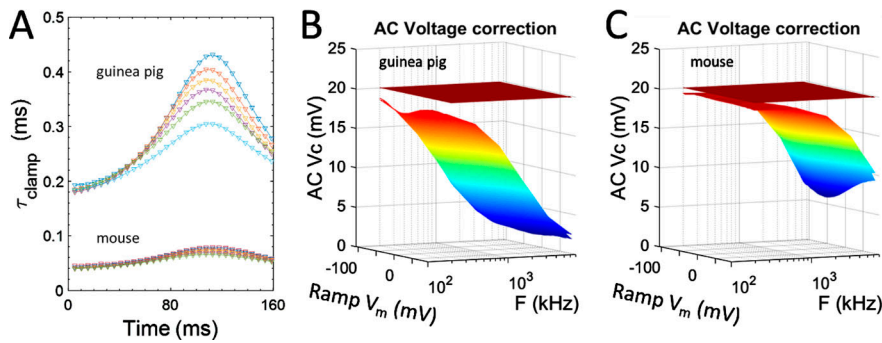


**Figure 2. Voltage roll-off corrections.** (A) Guinea pig and mouse OHC NLC is voltage-dependent and, as such, will influence the voltage clamp time constant, which is commonly calculated for whole-cell voltage clamp as  $\tau_{\text{clamp}} = R_s * C_m$ , or in our case,  $\tau_{\text{clamp}} = R_s * (C_{\text{lin}} + \text{NLC})$  (precisely,  $R_{\text{ij}} * [C_{\text{lin}} + \text{NLC}]$ ; see Materials and methods). The time constant is multifarious, and depends on holding voltage and frequency of stimulation. The voltage (or voltage-dependent eM) correction for the clamp time constant must be done at each stimulating frequency and holding voltage. (B and C) Complex whole-cell currents or calculated multifarious clamp time

constants were used to predict the roll-off in AC command voltage that actually excites the membrane (multicolored surface plots; see equations in Materials and methods). Each approach gives equivalent results. Note that because of the small size of mouse OHCs,  $\tau_{\text{clamp}}$  is faster than the guinea pig OHCs, and introduces better voltage delivery. Nevertheless, each must be corrected (brown flat surface plot, equivalent to command voltage) to ensure removal of voltage roll-off issues when analyzing eM data. F, frequency.

FFT of the whole ramped eM response was made, and shows that unlike the piezo-driven response (Fig. 1 B, panel 4), the magnitude of both guinea pig and mouse OHC eM falls precipitously with frequency. This roll-off arises from both the voltage-filtering effects of  $R_s$  and the kinetics of prestin and/or mechanical impediments to cell movements. In the following analysis, we restrict FFT inspection to defined integral segments (see the red and blue highlighted example regions in Fig. S1, Fig. S2, Fig. 3, and Fig. 4) of the eM ramp response to assess voltage dependence of the frequency response. Furthermore, we detail methods (see Materials and methods) to remove the effects of series resistance interference, thus revealing true eM frequency response as a function of true membrane voltage.

For the OHC under voltage clamp, we do not have direct access to the membrane voltage as in the model (see Materials and methods), so only two methods for eM correction are available—that using estimates of  $R_s$  and NLC to gauge  $\tau_{\text{clamp}}$ , and that using direct measures of whole-cell currents. In Fig. 2, complex whole-cell currents or calculated multifarious clamp time constants were used to predict the roll-off in AC command voltage (see equations in Materials and methods). Corrections will precisely account for the frequency-dependent roll-off in AC voltages and subsequently, the same corrections are applied to voltage-dependent eM measures.

We analyzed eight guinea pig OHCs. eM was commensurate with previously reported average eM gains of 15–19 nm/mV (Ashmore, 1987; Santos-Sacchi, 1989). Average ( $\pm$ SEM) Boltzmann parameters of NLC at the lowest frequency of 195 Hz are  $Q_{\text{max}}$ :  $3.18 \pm 0.06$  pC,  $V_h$ :  $-46.1 \pm 1.1$  mV,  $z$ :  $0.92 \pm 0.02$ , and  $C_{\text{lin}}$ :  $22.58 \pm 0.51$  pF.  $R_s$  was  $9.1 \pm 0.8$  M $\Omega$ .  $R_m$  at zero holding potential was  $401 \pm 75$  M $\Omega$ . Average eM gain evoked by the ramp protocol (Fig. 3 B) was  $22.8 \pm 2.8$  nm/mV. Maximum eM was  $2.54 \pm 0.32$   $\mu$ m; equivalent  $z$  was  $0.94 \pm 0.02$ . Fig. 3, E–G, surface and two-dimensional (2-D) plots, show average guinea pig OHC eM before and after correcting for  $R_s$ -induced voltage errors.

We also analyzed four mouse OHCs. Average ( $\pm$ SEM) Boltzmann parameters of NLC at the lowest frequency of 195 Hz are  $Q_{\text{max}}$ :  $0.74 \pm 0.02$  pC,  $V_h$ :  $-47.2 \pm 3.3$  mV,  $z$ :  $0.82 \pm 0.01$ , and  $C_{\text{lin}}$ :  $7.60 \pm 0.13$  pF.  $R_s$  was  $5.7 \pm 0.1$  M $\Omega$ .  $R_m$  at zero holding potential was  $239 \pm 53$  M $\Omega$ . Average eM gain evoked by the ramp protocol

(Fig. 4 B) was  $7.0 \pm 0.6$  nm/mV. Maximum eM was  $1.06 \pm 0.08$   $\mu$ m; equivalent  $z$  was  $0.70 \pm 0.03$ . Fig. 4, E–G, surface and 2-D plots, show average mouse OHC eM before and after correcting for  $R_s$ -induced voltage errors.

Fig. 3, E–G, and Fig. 4, E–G, illustrate that using either of the two possible correction approaches (Method 2 and Method 3) produces essentially the same results (in line with modeling in the figures in the Online supplemental material) and confirming the low pass nature of both guinea pig and mouse eM. Notably, the equivalence of the two methods also confirms the validity of the dual sine approach to measure high frequency capacitance, whose multifarious influence on clamp time constant must be considered in order to properly evaluate eM frequency response under voltage clamp.

In Fig. 5, A and B, we plot, at all interrogated frequencies, the voltage dependence of group-averaged eM gain and NLC for mouse and guinea pig OHCs. Guinea pig responses are lower pass than mouse responses. We additionally analyzed OHC response data individually, followed by averaging. Fig. 5, C and D, show mean and SEM of eM at  $V_h$ , and Boltzmann parameters of fits based on single cell analysis at frequencies spanning 195 to 3,125 Hz (mouse eM was additionally measured at 6,250 Hz). It is clear that the guinea pig eM frequency response is lower pass than the mouse response (quantification is shown in Fig. 6). It is noteworthy that guinea pig OHCs show a disparity between eM and NLC  $V_h$  that is not found in the mouse. Such disparity has been observed previously for guinea pig OHCs (Song and Santos-Sacchi, 2013; Duret et al., 2017), and we previously found that the disparity is diminished with increased turgor pressure for the guinea pig. For our mouse OHCs, we note that the cells appear substantially turgid (see Fig. 1 E), so this may be the reason for the absence in disparity in the mouse.

Fig. 6 shows eM and NLC cut-off frequencies ( $F_c$ ) for guinea pig and mouse. To approximate differences in frequency responses between NLC and eM for the mouse and guinea pig, we apply single Lorentzian fits to group-averaged eM and NLC within a restricted bandwidth (195–3,125 Hz) at each incremental holding potential of the ramped AC response. The cut-off frequencies display U-shaped dependencies on holding potential, AC voltage stimulation at  $V_h$  providing the slowest response.

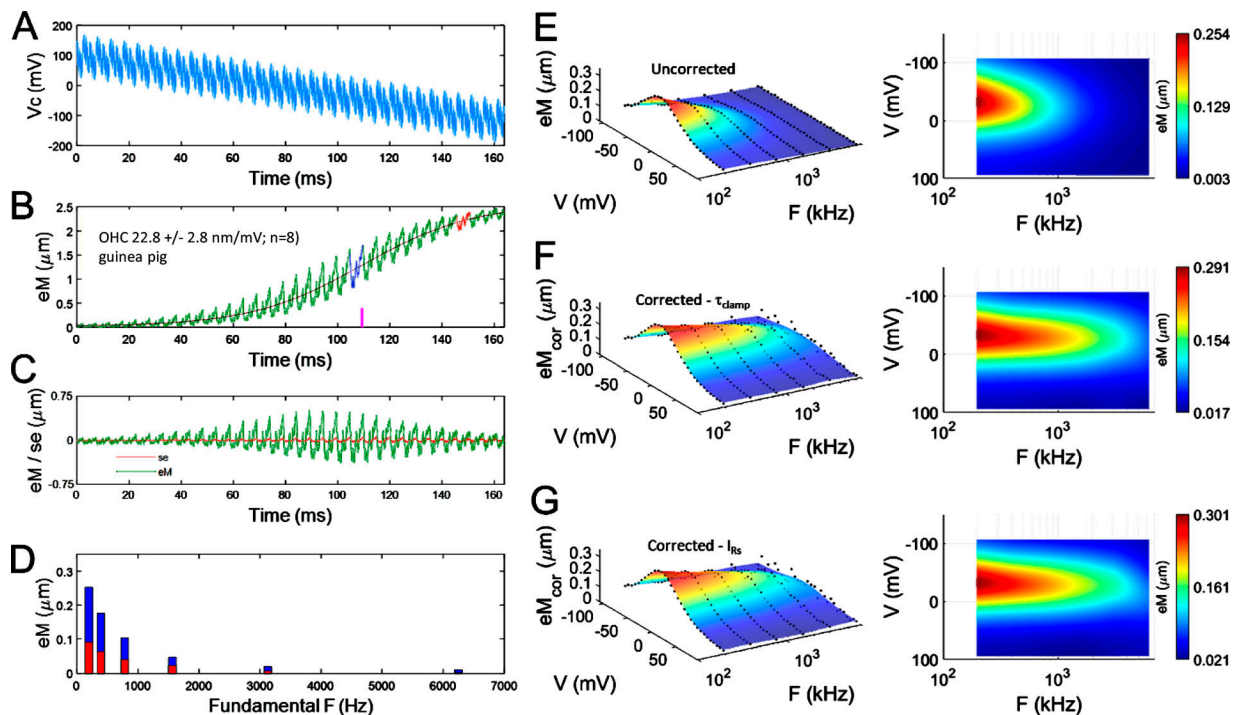


Figure 3. **Group-averaged guinea pig OHC eM frequency response corrected by two methods.** Data presented in A–E are pre-correction, and in F and G are after correction. **(A)** The hyperpolarizing ramp voltage stimulus (100 to –120 mV) with superimposed sum of 20 mV AC harmonic frequencies (195.3–6,250 Hz). A pedestal of 100 mV (81.32 ms) preceded the ramp. **(B)** Raw averaged eM. Two selected integral regions are highlighted. Blue is near  $V_h$  (magenta bar beneath shows position of  $V_h$ ). Red highlights a hyperpolarized region. **(C)** The eM data detrended (green) and the standard error (red). **(D)** Magnitude responses at the six interrogated frequencies of the two highlighted regions (colors correspond to those in B). Data were detrended as in C before FFT. The surface plots on the right provide a full analysis across ramp voltage at all integral regions of the eM data. **(E)** Uncorrected eM; the 2-D voltage frequency plots permit clearer visualization of the frequency responses. Black dots are data points. **(F)** eM adjusted with Method 3 based on corrections to multifarious  $\tau_{clamp}$  (see Materials and methods). **(G)** eM adjusted with Method 2 based on membrane current corrections, namely,  $V_m = V_c - I_{R_s} * R_{ij}$ . Note tight correspondence between the two approaches. These data indicate that OHC eM is low pass in nature.  $eM_{cor}$ , corrected eM.

eM corrections based on Methods 2 and 3 are overlapped, indicating accurate estimates of  $R_s$ . Individually analyzed cell averages (filled symbols with SEM, using Method 2) show good agreement with the group-averaged data. The  $F_c$  at  $V_h$  for guinea pig OHC eM is  $1.47 \pm 0.065$  kHz, and that for mouse OHC eM is  $4.26 \pm 0.74$  kHz. NLC measures follow this pattern, with cut-offs faster than that for eM. The  $F_c$  at  $V_h$  for guinea pig OHC NLC is  $2.47 \pm 0.091$  kHz, and that for mouse OHC NLC is  $6.83 \pm 0.46$  kHz.

To assess the frequency response of NLC under near ideal voltage clamp, we employed macro-patches of the guinea pig OHC lateral membrane. NLC measures were made using the ramp protocol, as above. Our video analysis setup was insufficient to measure patch movements induced by our ramped 20 mV AC stimuli. However, as with voltage-corrected whole-cell measures, patch NLC shows low-pass behavior (Fig. 7). At the lowest frequency of 195 Hz, fitted Boltzmann parameters of NLC are  $Q_{max}$ :  $38.6 \pm 6.1$  fC,  $V_h$ :  $-38.1 \pm 4.4$  mV, and  $z$ :  $0.67 \pm 0.03$ . No correction for resting potential was made for on-cell patch  $V_h$ .  $z$  is lower than whole-cell measures. For comparison, Gale and Ashmore (1997b), using a lock-in amplifier to measure NLC with 1 kHz sinusoids, found  $z$  to be 0.65 (slope factor  $\beta = 0.04$ ). Given our  $z$  and a hemispherical patch surface area (diameter equal to 3.5–4  $\mu\text{m}$ ), we calculate 3,851–5,030/ $\mu\text{m}^2$  elementary prestin motor units, in line with previous estimates.

Fig. 8 compares peak NLC from on-cell macro-patches with scaled values of whole-cell eM, NLC, and data from Gale and Ashmore (1997a). For frequency roll-off comparison, values were scaled to coincide with our macro-patch NLC values at 390.6 Hz. The roll-off of whole-cell eM and that of the patch movements measured by Gale and Ashmore are similar. The measures of peak NLC of whole-cell, macro-patch, and Gale and Ashmore’s patch NLC (points within our recording bandwidth are shown) are similar. The cut-off frequencies obtained with Lorentzian fits (either whole-cell or macro-patch data) show that eM and NLC frequency responses differ, with eM being slower, as noted above. We emphasize that the single Lorentzian fits here do not describe the full frequency response of NLC, but only that within our recording bandwidth. These measures are intended to make comparisons with our eM measures within the same recorded bandwidth. Thus, we conclude that the degree of coupling between prestin conformational changes (i.e., NLC) and eM must underlie differences between their frequency responses.

Finally, we observe that fits of the square root of eM provide cut-offs comparable to those for NLC for both mouse and guinea pig OHCs. The  $F_c$  at  $V_h$  for guinea pig OHC  $eM^{1/2}$  is  $2.77 \pm 0.11$  kHz, and that for mouse OHC  $eM^{1/2}$  is  $7.69 \pm 0.81$  kHz.  $t$  test comparisons to the cut-offs of NLC ( $2.47 \pm 0.091$  and  $6.83 \pm 0.46$ ,

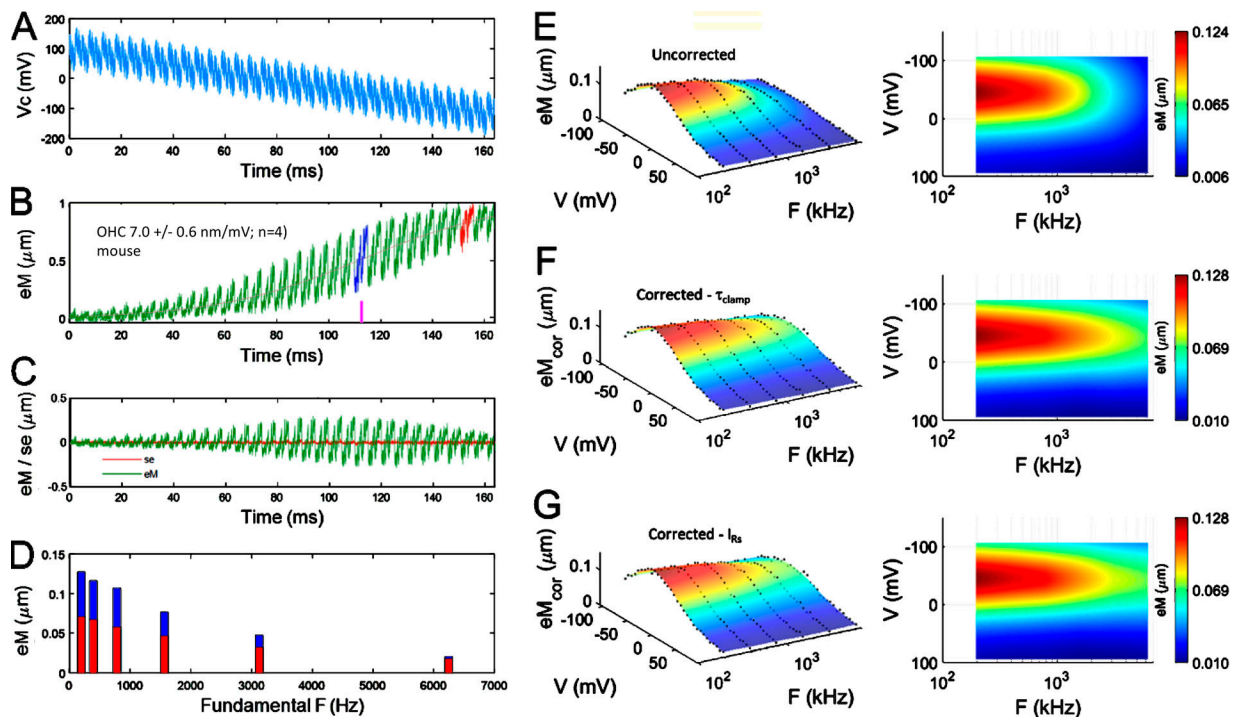


Figure 4. **Group-averaged mouse OHC eM frequency response corrected by two methods.** The caption of Fig. 3 directly applies to this figure. Note that the frequency extent of eM for the mouse is wider band than the guinea pig, before and after voltage corrections.

respectively) show no statistically significant differences ( $P = 0.1092$  and  $P = 0.4948$ , respectively). Below we consider the basis of such disparity.

## Discussion

Prestin works by sensing voltage with consequent alterations in its conformational state, leading to contractions and elongations of the cylindrical cell that provides enhancement of auditory threshold (Ashmore, 2008; Santos-Sacchi et al., 2017). Because of the large restricted prestin-generated charge movements evoked by voltage (Ashmore, 1990; Santos-Sacchi, 1991), a substantial alteration in membrane capacitance ensues, paradoxically altering the very voltage that the sensor senses. This is even expected to occur during normal acoustic stimulation, where the receptor potential will suffer from a multifarious membrane resistor-capacitor (RC) filter. For example, the receptor potential cut-off frequencies estimated using linear capacitance alone (Johnson et al., 2011) would be greatly reduced at  $V_h$ , where NLC can be as great as linear capacitance. In our study under voltage clamp, series resistance and membrane capacitance conspire to limit the imposition of voltage across the membrane, interfering in both time and magnitude. To evaluate effects of membrane potential across frequency, it is required to alleviate this interference. Here we have compensated for the multifarious time constants induced by  $R_s$  and NLC( $v, f$ ) in order to reveal the true voltage-induced frequency response of both guinea pig and mouse OHC eM across an array of holding potentials. Before proceeding, we review the literature on measures of eM frequency response.

## eM bandwidth studies

A review of OHC eM bandwidth studies has been published recently (Santos-Sacchi, 2019). Here we briefly review those studies with the aid of Table 1. Over the years, better techniques that have extended voltage delivery capabilities have provided increasingly higher estimates for eM cut-off frequencies. Of course,  $R_s$  of the patch pipette or the microchamber pipette, in combination with OHC capacitance, ultimately controls frequency delivery bandwidth under voltage clamp. Typically, the time course of the clamp can be garnered from exponential decays of current induced by voltage steps, but AC currents can also be used as we have done in our present work. Prior to Frank et al. (1999), eM cut-offs were typically below 10 kHz. Interestingly, Gale and Ashmore (1997a) measured both patch NLC and membrane movements, and found a NLC cut-off near 10 kHz, but a patch movement cut-off significantly lower (see Fig. 8). The reduced cut-off was attributed to mechanical impediments to patch movements, despite the expected coupling between charge movement and mechanical response. The introduction of the partitioning microchamber by Dallos and Evans essentially reduced membrane capacitance by delivering the voltage stimulus across the reduced series combination of the partitioned cell membrane capacitance (Dallos and Evans, 1995). Given membrane time constants that are equal for each partition, each will experience a flat delivery of a command voltage across the cell. However, the command voltage frequency response itself will be attenuated by the  $R_s * C_{in}$  filter,  $C_{in}$  being the input capacitance resulting from the series combination of partitioned capacitances (see microchamber

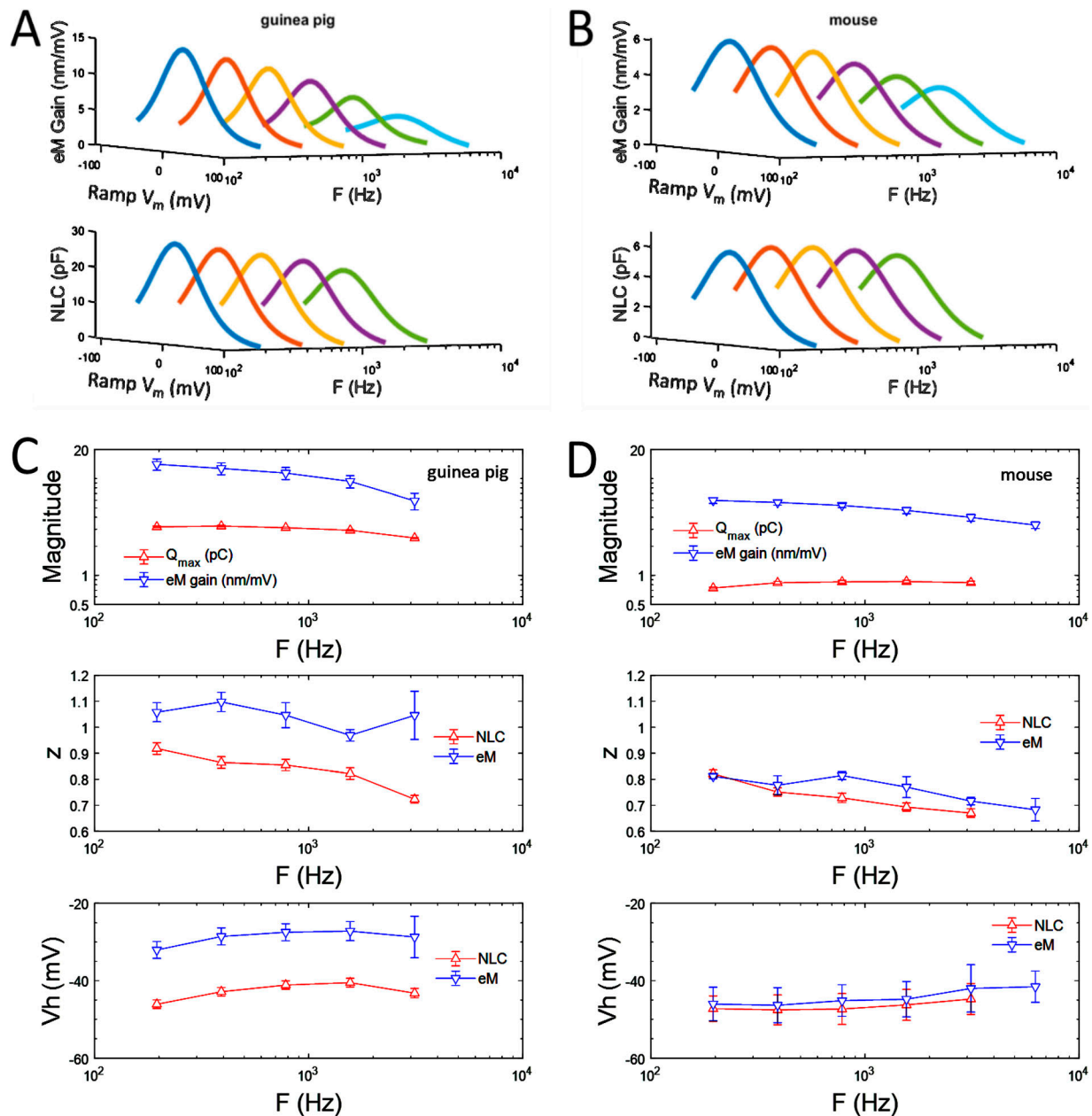


Figure 5. **Comparison of AC measured group-averaged guinea pig (A) and mouse (B) OHC NLC and associated eM frequency response as a function of holding voltage at each of the interrogated frequencies.** Neither mouse OHC NLC nor eM frequency response is as low pass as that of guinea pig OHC. These data were derived from cell averages of raw eM and membrane currents, as in Figs. 3 and 4. (C and D) Mean and SEM of eM at  $V_h$  and Boltzmann parameters of fits based on single-cell analysis. Note disparity of eM and NLC  $V_h$  and  $z$  for guinea pig as previously observed (Song and Santos-Sacchi, 2013). Mouse OHC eM and NLC  $V_h$ , on the other hand, are comparable.

schematic in Fig. 9 of Santos-Sacchi and Tan, 2018). Thus, Dallos and Evans, even though they did not monitor membrane currents to determine actual voltage roll-off, did estimate, given published OHC characteristics, the voltage delivery cut-off to be ~30 kHz in their experiments. This cut-off, as noted above, depended on their microchamber  $R_s$  and the input membrane capacitance. Of note for the studies by both Dallos and Evans and Frank et al., their zero microchamber offsets interrogated eM at holding membrane potentials far removed from  $V_h$ ; this is apparent from the small

eM gains reported compared with established eM gains between 15–19 nm/mV. Santos-Sacchi and Tan (2018) measured eM frequency response at two microchamber offsets, one near  $V_h$  and the other well offset from  $V_h$  (we estimate ~65 mV away). By measuring clamp tau from exponential decays at those two offsets, they found that eM is lower pass at  $V_h$ . Unfortunately, none of the previous studies have actually accounted for the voltage- and frequency-dependent roll-off of voltage delivery to the OHC, and without that correction, the true voltage-dependent eM frequency response remained unclear.



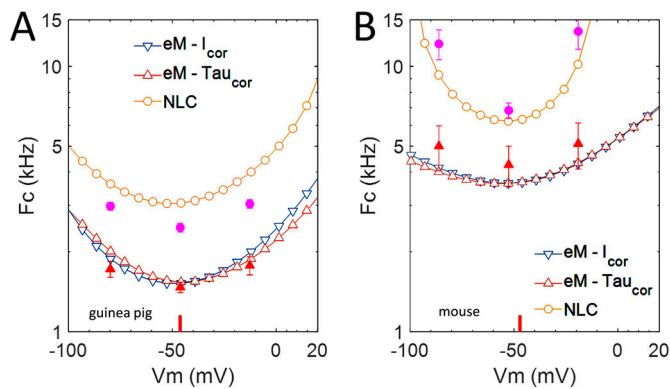


Figure 6. **Frequency cut-offs ( $F_c$ ) for NLC and eM.** (A and B) Single Lorentzian fits of NLC and associated eM data in Fig. 5, A and B. The plots show that the  $F_c$  of NLC and eM increases as ramp voltage deviates from  $V_h$ . The open symbols are from fits to averaged data. The cut-off frequency for each is a U shaped function of holding voltage, with NLC measures showing frequency cut-offs faster than that for eM. Using either of the two eM correction methods gives equivalent results (see Materials and methods section). The filled symbols with SEM are obtained from individually analyzed OHC data. The  $F_c$  at  $V_h$  for guinea pig OHC eM is  $1.47 \pm 0.065$  kHz, and that for mouse OHC eM is  $4.26 \pm 0.74$  kHz. The  $F_c$  at  $V_h$  for guinea pig OHC NLC is  $2.47 \pm 0.091$  kHz, and that for mouse OHC NLC is  $6.83 \pm 0.46$  kHz. The red bar on the voltage axis indicates NLC  $V_h$ .

### Similarities and differences between voltage-sensor movement (NLC) and eM

The electromechanical results we report on now explore the component of eM within 0.195–6.3 kHz, corresponding to human speech frequencies, and are made under whole-cell voltage clamp where, unlike the microchamber, precise DC and AC voltage delivery to the membrane is possible and predictable. Thus, we find with whole-cell recording, following voltage corrections due to the multifarious clamp time constant, that prestin's eM and NLC frequency response, in both mouse and guinea pig, exhibits low-pass electromechanical behavior within our measurement bandwidth. The frequency response is slowest at  $V_h$ , with a cut-off, approximated by single Lorentzian fits within that bandwidth, near 1.5 kHz for the guinea pig OHC and near 4.3 kHz for the mouse OHC, each increasing in a U-shaped manner away from  $V_h$ . NLC measures follow this U-shaped pattern.

By using macro-patch measurements, where voltage control is near ideal, we find that NLC frequency response is similar in roll-off to corresponding whole-cell measures within the speech frequency bandwidth, indicating our whole-cell voltage corrections were effective. Nevertheless, eM frequency cut-offs differ from those of NLC, which are faster. In OHC patches, Gale and Ashmore found that patch movement  $F_c$  was only 0.19 times that of NLC  $F_c$  (using the ratio of their reported corresponding tau values of 16 and 83.5  $\mu$ s for NLC and movements, respectively), which they attributed to interactions of prestin with cytoskeletal elements and viscous damping (Gale and Ashmore 1997a). That is, factors that influence prestin electromechanical behavior are present within the on-cell patch, i.e., intrinsic to the local environment of prestin within the membrane. Indeed, we have found physical and functional interactions of MAP1S, a small actin-binding protein, with prestin (Bai et al., 2010). However,

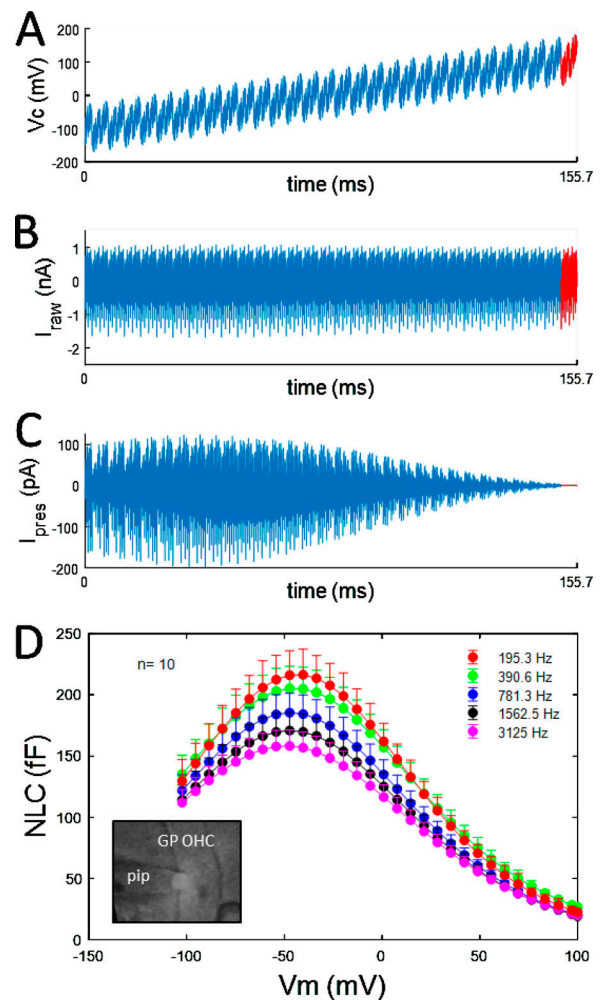
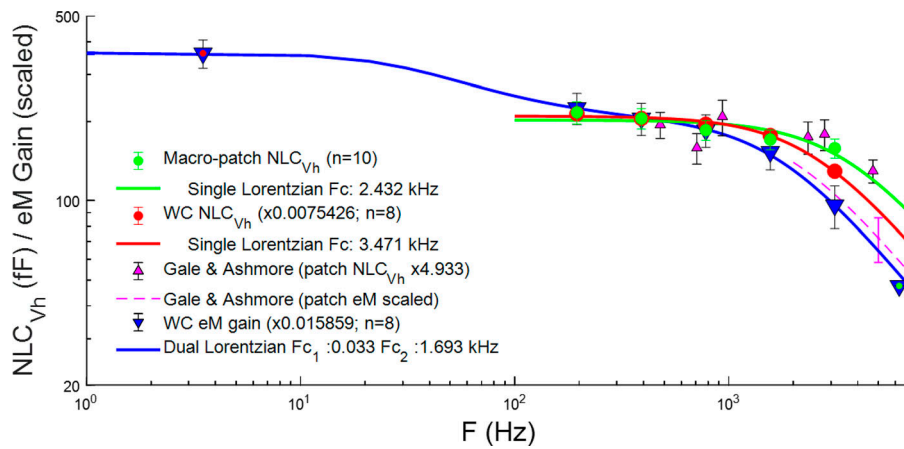


Figure 7. **Macro patches were made on the GP OHC lateral membrane to verify low pass behavior found in whole-cell measures of NLC.** (A) Command voltage; red highlighted regions used for stray and linear current subtractions; see Materials and methods). (B) Group-averaged currents recorded from on-cell macro-patches. Currents with AC components removed were used for detrending AC responses before highlighted region subtraction and FFT. (C) Resulting prestin-associated nonlinear currents. (D) Patches were individually analyzed to obtain NLC derived from nonlinear currents. Inset shows a patched OHC lateral membrane. Diameter of the OHC is 10  $\mu$ m. Mean  $\pm$  SEM. Pip, patch pipette;  $I_{raw}$ , raw current; fF, femtofarads;  $I_{pres}$ , prestin currents.

such influential effects on eM might be expected to work on both eM and NLC, since charge movement and mechanics are coupled (Dong and Iwasa, 2004; Santos-Sacchi and Tan, 2018). Consequently, the discrepancy between eM and NLC frequency response that is observed must point to variability of coupling charge movement to eM. Of course, uncoupling is clearly observable by deflating the OHC, which preserves NLC while abolishing whole-cell eM (Santos-Sacchi, 1991). Thus, we suggest that a variable coupling between whole-cell mechanics and prestin activity limits OHC influences on cochlear amplification at high frequencies. To this point, Vavakou et al., 2019 have recently observed limited, low-pass estimates of OHC eM frequency response using optical coherence microscopy vibrometry in the high-frequency region of the living gerbil.



**Figure 8. Comparison of macro-patch peak NLC frequency response with whole-cell responses and published data (eM and NLC).** Data are scaled to macro-patch NLC at 390.6 Hz to compare frequency roll-off. Whole-cell NLC and macro-patch NLC both show low pass behavior. A single Lorentzian fit of the macro-patch (green) and whole-cell (red) NLC, indicates low pass behavior for each that is faster than whole-cell eM cut-off. For comparison, the roll-off of patch movement measures of [Gale and Ashmore \(1997a\)](#); purple dashed line being the equivalent Lorentzian of their movement tau and the purple SEM error bar depicting the equivalent mean  $\pm$  SEM response at 5 kHz; scaled in magnitude to over lie our eM roll-off) are plotted, and roll-off appears similar to that of our whole-cell eM. Gale and Ashmore's patch NLC data (their points

within our measurement bandwidth) are comparable to our macro-patch measures. The downward blue triangle with a red dot is derived from the ramp eM gain ([Fig. 3 B](#)), and that with the light blue dot is from group-averaged responses ([Fig. 5 A](#)). Overall, the figure shows the discrepancy between eM and NLC roll-off, with NLC presenting a higher frequency cut-off. Mean  $\pm$  SEM. WC, whole cell.

### What factors may influence OHC eM frequency response?

Within our interrogation bandwidth, NLC and eM are low pass. Since we accurately corrected for voltage delivery roll-off, the differential eM roll-off must result from other factors intrinsic and/or extrinsic to the cell. Two features require exploration not previously considered. One is the mechanism for voltage dependence of the cut-off frequency,  $F_c$  ([Fig. 6](#)). The other is a discrepancy in  $F_c$  for NLC and eM. The values of  $F_c$  for NLC are higher than those of eM. That is, eM appears to be low-pass filtered.

There are two factors that contribute to the frequency dependence that we measure. One is due to the intrinsic transition rates between prestin's conformational states ([Iwasa, 1997](#)). Another factor, which is extrinsic to the motile element itself, is due to mechanical loads imposed on both the cell and the motile element. In the absence of mass, the characteristic frequency is determined by viscoelastic relaxation.

Mechanical factors could lead to a voltage dependence of  $F_c$  if the axial stiffness of the cell is itself voltage dependent, because the characteristic frequency of viscoelastic relaxation is determined by  $k/\eta$ , where  $k$  is the axial stiffness and  $\eta$  the drag coefficient. Indeed, it has been reported that the axial stiffness significantly decreases on deep depolarization ([He and Dallos, 1999, 2000](#)). Such a reduction in stiffness leads to a lower viscoelastic frequency as holding voltage is moved away from  $V_h$ , and is inconsistent with our observations. On the other hand, an alteration of axial stiffness has been theoretically predicted as an analogue of "gating compliance," in which conformational transitions contribute to length changes of the cell ([Iwasa, 2000](#)). The predicted voltage dependence of the compliance, the inverse of stiffness, is bell-shaped, similar to NLC and qualitatively similar to our observed  $F_c$  values. Nevertheless, this effect is much too small to account for our observations. Actually, the magnitude of the "gating compliance" is quantitatively consistent with a report that voltage dependence of axial OHC stiffness is absent ([Hallworth, 2007](#)). Indeed, a previous treatment of a viscoelastic process involving the OHC does not lead to voltage dependence of the viscoelastic frequency for a

voltage driven stimulus, while it does for a force stimulus ([Iwasa, 2016](#)).

A stochastic transition model, even the simplest two-state model, inherently predicts voltage dependence because the characteristic frequency is expressed as a sum of transition rates in opposite directions from the distribution's midpoint ([Iwasa, 1997](#)). In one direction, the rates increase exponentially with larger depolarizations, and in the other direction with larger hyperpolarizations, similar to the  $F_c$  values in [Fig. 6](#).

Disparate frequency dependence for NLC and eM is a new observation, and there is no previous theoretical prediction or explanation. This is because it has been assumed that the cell undergoes the same mode of motion as the motile element. For a model in which eM is the low-pass filtered output of the motile element, it is possible to obtain different values of  $F_c$  for NLC and eM.

To capture the essential features of the observed high-frequency behavior of NLC and that of eM, we examined various mechanical loads assuming two conformations for the motile element (see Appendix). Virtually all kinetic models of prestin thus far reported, including the *meno presto* model ([Santos-Sacchi and Song, 2014a](#)), use this two-state formalism for eM and NLC generation.

We found that our experimentally observed eM and NLC frequency dependence can be explained by assuming that the motile element, which undergoes stochastic transitions, drives a mechanical system with two modes of motion. More specifically, cell displacement is the low-pass filtered output of the motile element displacement (see Appendix). The schematic configuration of the mechanical model is shown in [Fig. 9](#). The model is constructed based on likely mechanical interactions within and external to the OHC. Thus, we view the elements  $k_2$ ,  $\eta_2$ , and  $k_1$  as representing the local environment, consisting of the lateral plasma membrane and cytoskeletal structures, surrounding the motile element (P). The elements  $k_0$  and  $\eta_0$  represent parts of the cell distant from the given motile element, primarily involved in energy dissipation due to the drag against the external medium. The existence of the elastic element  $k_0$  may indicate

Table 1. History table of OHC eM frequency measurements

Publication	Method to evoke and measure load-free eM	Frequency response cut-off	Voltage delivery and/or eM measurement limitations	Notes
(Kachar et al., 1986)	Transcellular AC current; standard video	No estimate of roll-off; 1–30 Hz frame rates.	$R_m * C_m$ time constant; limited to 60 frames/s	
(Ashmore, 1987)	Whole-cell voltage clamp; photodiode	Dual Lorentzian cut-offs at 67 and 664 Hz	Voltage clamp $R_s * C_m$ time constant	
(Santos-Sacchi, 1992)	Whole-cell voltage clamp; photodiode	Single Lorentzian cut-off at 1 kHz	Voltage clamp $R_s * C_m$ time constant	
(Reuter et al., 1992)	Transcellular AC current stimulation in organ explants; stroboscopic video	40 dB down at 15 kHz	Membrane $R_m * C_m$ time constant	
(Dallos and Evans, 1995)	Microchamber cell partitioning, AC voltage from low-impedance waveform generator; photodiode	No estimate of roll-off, as shape of frequency response is a function of apical to basal impedances; eM detection above 10 kHz; zero microchamber V offset	$R_s * C_{in}$ (input capacitance of partitioned cell) for command voltage; ratio of partitioned impedance modifies roll-off shape	Low frequency eM gain: ~5 nm/mV indicative of offset away from $V_h$ ; no estimation of V delivery roll-off based on generated currents
(Gale and Ashmore 1997b)	On-cell and excised membrane patch under voltage clamp	Patch movements ( $\approx$ eM) measured with step voltages; 10 kHz cut-off for patch NLC; 0.19 $\times$ lower cut-off for movements	Near ideal voltage clamp	First indication that eM and NLC frequency response may differ
(Frank et al., 1999)	Microchamber cell partitioning; voltage clamp; laser Doppler vibrometer	Variable cut-off; for 30 $\mu$ m cell extrusion 33 kHz; smaller extrusions > 70 kHz; zero microchamber V offset	$R_s * C_{in}$ for command voltage; ratio of partitioned impedance modifies roll-off shape	Low frequency eM gain: ~5 nm/mV indicative of offset away from $V_h$ ; voltage corrections based on $R_s * C_{in}$ (stray    membrane capacitance)
(Kitani et al., 2011)	Transcellular AC current; video analysis at 18 kHz	Responses measured up to 4 kHz	$R_m * C_m$ time constant	Time dependent changes in eM magnitude may be attributed to mechanisms other than prestin
(Santos-Sacchi and Tan, 2018)	Microchamber cell partitioning; voltage clamp; video analysis at 50 KHz frame rate	At microchamber V offset to $V_h$ , dual Lorentzian cut-offs of 33 Hz and 6.3 kHz; at zero microchamber V offset, dual Lorentzian cut-offs of 234 Hz and 8.7 kHz	$R_s * C_{in}$ for command voltage; ratio of partitioned impedance modifies roll-off shape	Low frequency eM gain (at $V_h$ ): 16.8 nm/mV; voltage corrections based on exponential current decays during V stimulation at two microchamber offsets; eM measures made under whole cell voltage clamp were not corrected for delivery roll-off

that the drag is not concentrated at a single location, but it is distributed along the cellular axis.

Small mechanical displacements,  $x$  and  $y$ , elicited by small sinusoidal voltages with frequency  $f$  applied on the motile element, can be expressed as (see derivation in Appendix),

$$x(f) = \frac{k_{12} \gamma(f)}{k_{02} + k_{12} + i f / f_1}, \quad (10a)$$

$$\gamma(f) = \frac{\beta \bar{P}_{\pm} a q N}{1 + f / f_g} \cdot \frac{\nu}{k_{12}^2 (k_{01} + k_{12} + i f / f_1) - (k_{12} + i f / f_2)}, \quad (10b)$$

where  $f_g$  is the gating frequency,  $k_{02} = k_0/k_2$ ,  $k_{12} = k_1/k_2$ ,  $2\pi f_0 = \eta_0/k_2$ , and  $2\pi f_2 = \eta_0/k_2$ . Here,  $i = \sqrt{-1}$ . The voltage dependence of the magnitude of these quantities is determined by  $\bar{P}_{\pm}$ , which is proportional to NLC at low frequencies (see Appendix). Notice here that NLC is associated with  $x$ , and eM with  $\gamma$ . Eq. 10a indeed shows that  $x$  is a low-pass filtered output of  $\gamma$ .

Importantly, the model captures two features of our experimental observations. One is the voltage dependence of  $F_c$  due to

gating frequency  $f_g$ . The other is that the roll-off of eM takes place at lower frequency than that of NLC.

Fig. 10 shows model fits of experimentally determined eM and NLC frequency responses at three holding potentials, passing through  $V_h$ . The parameter values obtained by simultaneous data fit at each holding voltage appear reasonable. However, standard errors are large, mainly due to the dependency between the substantial number of parameters. Such an example is shown in Fig. 10 A, which shows plots using two sets of parameter values, where the stiffness ratios of one set are larger than the other by about fivefold. For this reason, it is unlikely that the present analysis can provide definitive information regarding the axial stiffness of OHCs. Nevertheless, Fig. 10 indicates that the gating frequency  $f_g$  obtained at each holding voltage is consistent with the stochastic model with the lowest value, namely near  $V_h$  (at  $-45.8$  mV). That is, the values of  $f_g$  distinctly characterize the plots at each holding voltage, while the values for the remaining parameters remain essentially the same.

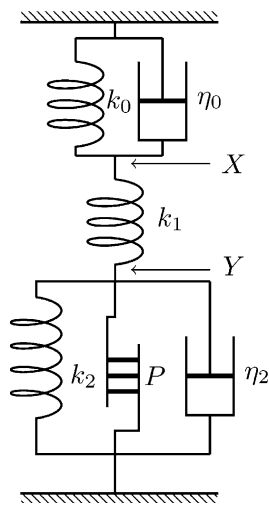


Figure 9. **Schematic diagram of mechanical load on the motile element.** Mechanical load consists of three elastic elements  $k_0$ ,  $k_1$ , and  $k_2$ , and two dashpots  $\eta_0$  and  $\eta_2$ .  $X$  represents the displacement of the cell, and  $Y$  indicates the displacement of the motile element, labeled as  $P$ .

### Summary

The relationship between OHC resting potential and NLC  $V_h$  will govern the frequency response of eM. We previously proposed that a mismatch between resting potential and NLC  $V_h$  could enhance the frequency response of eM through a gain-bandwidth adjustment (Santos-Sacchi and Tan, 2018). Our new data are in line with this proposal and provide a detailed description of the OHC's electromechanical cut-off frequency across voltage in both guinea pig and mouse OHCs. This cut-off frequency is U-shaped about  $V_h$ , and increases as holding voltage deviates from  $V_h$ . Importantly, the eM voltage dependence is mirrored by that of NLC, though frequency cut-offs differ. The cut-off disparity likely results from the influences of internal and external loads upon the motile mechanism. In this regard, we should comment on the observed differences in  $F_c$  values for mouse and guinea pig. Do differences in intrinsic prestin

kinetics exist between mouse and guinea pig, as the viscoelastic model might suggest? While preliminary, we have macro-patch measures out to 20 kHz that indicate similar prestin kinetics in the two species. That is, we explored the frequency response of NLC in patches from mouse and guinea pig OHC lateral membranes, each showing low-pass, stretched exponential behavior with roll-offs at half magnitude near 10–12 kHz at room temperature (unpublished data). In this light, we expect that the structural differences between the two species' cells (e.g., length, diameter) may have provided differing loads on prestin with consequential differences in eM and NLC, given that the piezoelectric nature of prestin will be affected by load. In sum, all of our observations indicate that the influence of OHC activity on cochlear amplification is more complicated than has been envisioned.

Finally, we note that the kinetics of prestin are readily monitored through shifts in  $V_h$ , a reflection of the ratio of forward to backward transition rates. These kinetics, a determining factor in eM frequency response, depend on a host of other factors, including intracellular chloride, membrane tension and thickness, and temperature (Iwasa, 1993; Gale and Ashmore, 1994; Meltzer and Santos-Sacchi, 2001; Oliver et al., 2001; Santos-Sacchi et al., 2001; Izumi et al., 2011; Santos-Sacchi and Song, 2016). Indeed, alterations in prestin kinetics have been found in mutations in prestin (Homma et al., 2013). We suspect that eM frequency response is not a static feature in vivo.

## Appendix

### Rate equations for membrane molecules with mechanoelectric coupling: Introduction

There are two kinds of theories for describing the frequency dependence of cells with motile elements based on mechano-electric coupling. One of them is based on kinetic equations with intrinsic transition rates, which have been used to describe conformational changes of proteins, such as ion transporters (Kolb and Lauger, 1978), ignoring the effect of mechanical load imposed on those cells (Iwasa, 1997).

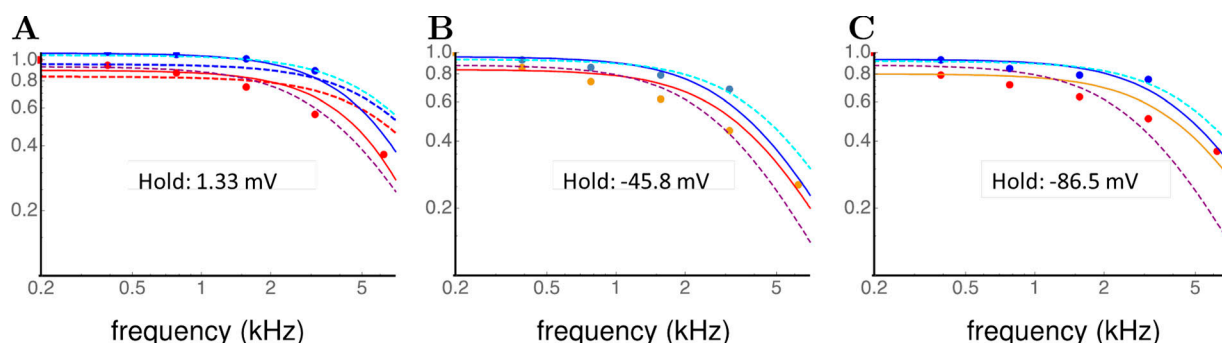


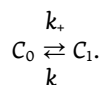
Figure 10. **Frequency dependence of NLC and eM.** Comparison with model predictions. Blue data points represent NLC and red data points eM. Solid lines indicate simultaneous fit for NLC and eM with the model at each holding potential. The color coding is the same as for the data points. Dashed lines in cyan and purple represent Lorentzian fit, respectively, for NLC and eM data. **(A)** Holding potential 1.33 mV; fit parameters are  $f_g = 7.86$  kHz,  $f_1 = 23.4$  kHz,  $f_2 = 69.9$  kHz,  $k_0/k_2 = 0.58$ , and  $k_1/k_2 = 0.26$ . **(B)** Holding potential  $-45.8$  mV,  $f_g = 3.97$  kHz,  $f_1 = 29.5$  kHz,  $f_2 = 80.6$  kHz,  $k_0/k_2 = 3.82$ , and  $k_1/k_2 = 1.31$ . **(C)** Holding potential  $-86.5$  mV,  $f_g = 5.14$  kHz,  $f_1 = 38.1$  kHz,  $f_2 = 74.3$  kHz,  $k_0/k_2 = 4.37$ , and  $k_1/k_2 = 1.60$ . At 1.33 mV (in A), the best fit stiffness ratios are different from at other voltages. To examine the effect of difference in the stiffness ratios, additional dashed lines are drawn in blue and red, respectively, for NLC and eM, where the parameter values for B are used, except for the gating frequency  $f_g$ , which is set at 7.86 kHz.

Another kind of treatment assumes that intrinsic conformational transitions are infinitely fast. Conformational transitions are determined by the equation of motion for these cells, on which mechanical load is imposed (Iwasa, 2016). The resulting frequency responses of these cells are characterized by mechanical factors, such as the resonance frequency and the frequency for viscoelastic relaxation.

The present treatment introduces the dependence on mechanical load into the conformational transition rates, enabling description of the general case, where the intrinsic transition rates are finite. Two previous theories are recovered as special cases. In addition, we examine how mechanical complexity of the system can give rise to discrepancy in the frequency dependence of nonlinear capacitance NLC and that of motile response. For simplicity, we assume that the motile molecule has two discrete conformational states. The terms “motile molecules” and “motile element” are used interchangeably.

### Motile element with two states

Consider a membrane molecule with two discrete conformational states,  $C_0$  and  $C_1$ , and let the transition rates  $k_+$  and  $k_-$  between them be schematically expressed as



Let  $P_1$  be the probability that the molecule in state  $C_1$ . Then, the probability  $P_1$  can be expressed by the transition rates

$$\frac{P_1}{1 - P_1} = \frac{k_+}{k_-} = \exp[-\beta q(V - V_0)], \quad (A1)$$

where  $q$  is the charge transferred across the membrane during conformational changes,  $V$  the membrane potential,  $V_0$  a constant, and  $\beta = 1/k_B T$  with the Boltzmann constant and  $T$  the temperature.

If  $q$  is positive, the energy level of the state  $C_1$  is higher, reducing  $P_1$  as the membrane potential  $V$  rises. For prestin in outer hair cells, which shorten on depolarization, if we choose  $C_1$  as the shortened state, the unit length change  $a$  on conformational change is negative, and then we have  $q < 0$ . Notice that the quantity  $a$  does not appear in Eq. A1.

The transition rates that satisfy Eq. A1 can be given by

$$k_+ = \exp[-\alpha\beta q(V - V_0)], \quad (A2)$$

$$k_- = \exp[(1 - \alpha)\beta q(V - V_0)], \quad (A3)$$

where  $\alpha$  is an arbitrary constant.

The time dependence of  $P_1$  can be expressed by the rate equation

$$\frac{d}{dt}P_1 = k_+ - (k_+ + k_-)P_1. \quad (A4)$$

Now we introduce sinusoidal voltage changes of small amplitude  $v$  on top of constant voltage  $\bar{V}$ , i.e.,  $V = \bar{V} + v \exp[i\omega t]$ , where  $\omega$  is the angular frequency and  $i = \sqrt{-1}$ . Then the transition rates are time-dependent due to the voltage dependence Eq. A1. They satisfy

$$\frac{k_+}{k_-} = \frac{\bar{k}_+}{\bar{k}_-} (1 - \beta q v \exp[i\omega t]). \quad (A5)$$

Notice  $\bar{k}_+$  and  $\bar{k}_-$  are time independent, and we assume that  $v$  is small so that  $\beta q v \ll 1$ . A set of  $k_+$  and  $k_-$  that satisfies Eq. A5 can be expressed

$$k_+ = \bar{k}_+ (1 - \alpha\beta q v \exp[i\omega t]), \quad (A6)$$

$$k_- = \bar{k}_- \{1 - (1 - \alpha)\beta q v \exp[i\omega t]\}. \quad (A7)$$

If we express  $P_1 = \bar{P}_1 + p_1 \exp[i\omega t]$ , we have respectively for the 0th and first order terms (Iwasa, 1997)

$$\bar{P}_1 = \frac{\bar{k}_+}{\bar{k}_+ + \bar{k}_-}, \quad (A8)$$

$$p_1 = -\frac{\bar{k}_+ \bar{k}_-}{\bar{k}_+ + \bar{k}_-} \cdot \frac{\beta q v}{i\omega + \bar{k}_+ + \bar{k}_-}. \quad (A9)$$

Notice that  $p_1$  does not depend on the factor  $\alpha$ .

Eq. A9 leads to voltage-driven mechanical displacement  $a p_1 \exp[i\omega t]$  with

$$a p_1 = -\bar{P}_\pm \cdot \frac{\beta a q v}{1 + i\omega/\omega_g}, \quad (A10)$$

where  $\bar{P}_\pm = \bar{P}_1(1 - \bar{P}_1)$ . The amplitude  $|x|$  of the motile response is given by

$$|x|^2 = \frac{(\beta a q \bar{P}_\pm)^2}{1 + (\omega/\omega_g)^2} \cdot v^2. \quad (A11)$$

Charge displacement is expressed by  $q p_1$  and the contribution to complex admittance  $Y(\omega)$  is given by  $(q/v)(d/dt)p_1 \exp[i\omega t]$  (Iwasa, 1997). The contribution to the membrane capacitance is  $C_{nl}(\omega) = \text{Im}[Y(\omega)]/\omega$  and therefore

$$C_{nl}(\omega) = \frac{\beta q^2 \bar{P}_1(1 - \bar{P}_1)}{1 + (\omega/\omega_g)^2}. \quad (A12)$$

This contribution to the membrane capacitance is commonly referred to as NLC because it shows marked voltage dependence. Notice also that the above derivation evaluates the contribution of a single unit of motile element. For a cell that contains  $N$  motile units, both  $|x|$  and  $C_{nl}$  need to be multiplied by  $N$ .

The roll-off frequency  $\omega_g$  due to gating is expressed by  $\omega_g = \bar{k}_+ + \bar{k}_-$ , which is voltage dependent. Using Eqs. A2 and A3, we obtain

$$\omega_g = \exp[-\alpha\beta q(\bar{V} - V_0)] + \exp[(1 - \alpha)\beta q(\bar{V} - V_0)]. \quad (A13)$$

This means that  $1/\omega_g$  rises at both ends of the membrane potential because  $\alpha$  can take any value between 0 and 1. That means  $\omega_r$  can be asymmetric unless  $\alpha = 1/2$ .

In the special case of  $\alpha = 1/2$ ,  $k_+ = 1/k_-$ . If we define  $b(V) = \exp[-\beta q(\bar{V} - V_0)/2]$ , then

$$1/\omega_g = 1/[b(V) + 1/b(V)], \quad (A14)$$

which resembles the bell-shaped voltage dependence of nonlinear capacitance at low frequencies ( $\omega \rightarrow 0$ ).

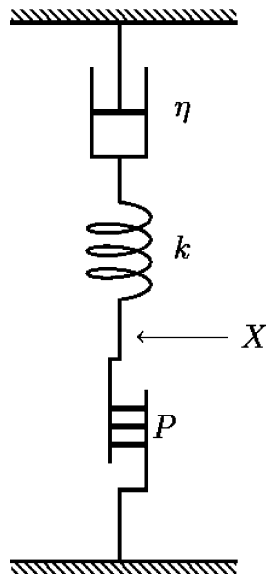


Figure A1. **Schematic representation of a cell with viscous drag.** The stiffness of the cell is  $k$ , and drag coefficient is  $\eta$ . The motile element is labeled  $P$ . The mechanical displacement of the cell is represented by  $X$ .

**Mechanoelastic coupling**

For motile membrane proteins based on mechanoelectric coupling, charge transfer is affected by mechanical factors. Here, we assume the cell is cylindrical as in the case of cochlear outer hair cells and approximate it as a one-dimensional object (Fig. A1).

Supposing charge transfer  $q$  is associated with a change  $a$  in the length of the cell, Eq. A1 should be replaced by

$$\frac{P_1}{1 - P_1} = \frac{k_+}{k_-} = \exp[-\beta[q(V - V_0) + aF]], \tag{A15}$$

where  $F$  is the axial force on the cell. The revised transition rates  $k_+$  and  $k_-$  also depend on the mechanical factor

$$K_+ = \exp\left[-\alpha \frac{\beta}{2}[q(V - V_0) + aF]\right], \tag{A16}$$

$$k_- = \exp\left[(1 - \alpha) \frac{\beta}{2}[q(V - V_0) + aF]\right]. \tag{A17}$$

For the rest of the present paper, the dependence on the value of the parameter  $\alpha$  does not appear except for  $\omega_g$ .

With a shorthand notation  $\bar{P}_\pm (= \bar{P}_1(1 - \bar{P}_1))$ , the change of the conformational probability  $p_1$  can be driven either by changes in the voltage as well force:

$$p_1 = -\beta \bar{P}_\pm \frac{qv + af}{1 + i\omega/\omega_g}. \tag{A18}$$

If the motile element is driven by voltage changes,  $p_1$  is proportional to  $v$  and mechanical displacement is given by  $ap_1$ .

**Effect of viscous drag**

Movement is driven by a deviation from Boltzmann distribution. When voltage changes with amplitude  $v$  imposed,  $p_1$  as expressed by Eq. A18 is the goal of the drive. Since this force is countered by viscous drag (with drag coefficient  $\eta$ ), the equation of motion in the frequency domain can be expressed by

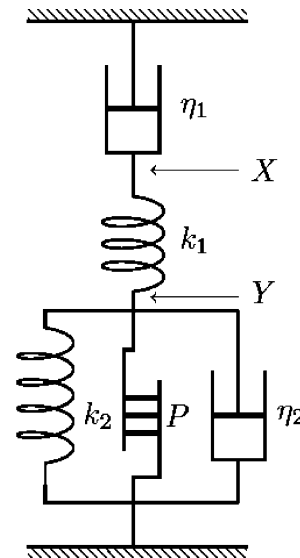


Figure A2. **Schematic representation of a cell with complex mechanical relaxation.** The local relaxation process associated with the motile element  $P$  is characterized by a spring with stiffness  $k_2$  and a dashpot with drag coefficient  $\eta_2$ . The local displacement is expressed by  $Y$ . The global relaxation process is characterized by a spring  $k_1$  and a dashpot with drag coefficient  $\eta_1$ . The cellular displacement is expressed by  $X$ .

$$i\eta\omega ap = ka(p_1 - p). \tag{A19}$$

Notice here that the equilibrium transition rates here depend not only on  $\bar{V}$  but also on  $\bar{F}$  because the motile element based on piezoelectricity is sensitive to mechanical force as well as the membrane potential.

Eq. A19 leads to

$$(1 + i\omega/\omega_\eta)p = -\frac{\beta \bar{P}_\pm}{1 + i\omega/\omega_g} \cdot qv, \tag{A20}$$

similar to the previous treatment for the special case without inertial loading (Iwasa, 2016). Here, the viscoelastic relaxation frequency is defined by  $\omega_\eta = k/\eta$ . It is essentially an equation for viscoelastic relaxation, adding a low pass filter to the motile mechanism. It is consistent with previous expressions in both extremes, i.e.,  $\omega_g \rightarrow \infty$  and  $\omega_\eta \rightarrow \infty$ .

The voltage dependence of NLC and that of motile response are identical. In the following, we show that mechanical load with complex relaxation can lead to discrepancy in their frequency dependences.

**Complex mechanical relaxation**

Let  $X$  represent the point that links a spring  $k_1$  with a dashpot  $\eta_1$ . Let  $Y$  represent the point that joins the spring  $k_1$  with the rest, which includes a spring  $k_2$ , a dashpot  $\eta_2$ , and a driver (Fig. A2). The equations of motion of this system driven by force  $F$  generated at the location  $P$  can be expressed

$$\eta_1 \frac{dX}{dt} = -k_1(X - Y), \tag{A21}$$

$$F + k_2Y + \eta_2 \frac{dY}{dt} = k_1(X - Y). \tag{A22}$$

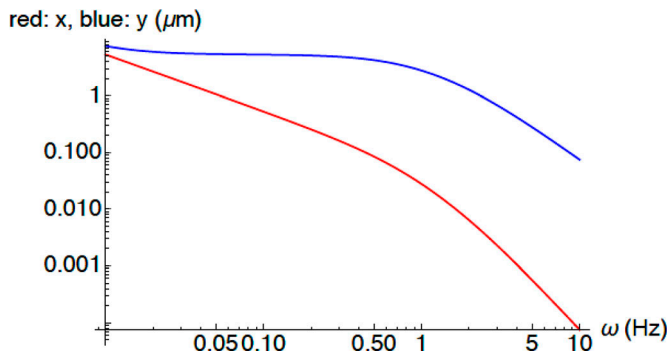


Figure A3. An example of the frequency dependence of  $x$  (red) and  $y$  (blue). Parameter values:  $\omega_g = 2$ ,  $\omega_1 = 0.01$ ,  $\omega_2 = 5.12$ , and  $\frac{k_1}{k_2} = 0.16$ .

If the force generator operates at a frequency  $\omega$  with small amplitude on top of its steady value  $\bar{F}$ ,  $F = \bar{F} + f \exp[i\omega t]$ . By letting the small amplitude components of  $X$  and  $Y$  with frequency  $\omega$  be represented by  $x$  and  $y$ , Eqs. A21 and A22 turn into

$$i\omega\eta_1 x = -k_1(x - y), \tag{A23}$$

$$f + (k_2 + i\omega\eta_2)y = k_1(x - y). \tag{A24}$$

Eq. A23 can be rewritten as

$$x = \frac{y}{1 + i\omega/\omega_1}, \tag{A25}$$

which indicates that the quantity  $x$  is obtained by low-pass filtering  $Y$  with roll-off frequency of  $\omega_1 (= k_1/\eta_1)$ .

By introducing a characteristic frequency,  $\omega_2 (= (k_1 + k_2)/\eta_2)$ , Eq. A24 can be transformed into

$$f + (k_1 + k_2)[1 + i\omega/\omega_2]y = k_1x. \tag{A26}$$

Elimination of  $x$  from Eq. A26 with the aid of Eq. A25 leads to

$$y = f/G_1(\omega), \tag{A27}$$

$$G_1(\omega) = \frac{k_1}{1 + i\omega/\omega_1} - (k_1 + k_2)(1 + i\omega/\omega_2). \tag{A28}$$

An approach analogous to those in the previous sections lead to an equation

$$G_1(\omega)ap = ak_2(p_1 - p). \tag{A29}$$

Since we have  $y = ap$ , this equation leads to

$$[G_1(\omega) + k_2]y = \frac{\beta\bar{P}_\pm k_2 a q v}{1 + i\omega/\omega_g}. \tag{A30}$$

Eqs. A25 and A30 show that the relationship between  $y$  and  $v$  has three adjustable parameters,  $\omega_1$ ,  $\omega_2$ , and  $k_r (= k_1/k_2)$ . For an example of the frequency dependence of  $y$ , see Fig. A3.

The frequency dependence of NLC is the same as that of  $y$ . Motile response  $x$  is obtained by low-pass filtering  $y$ . The roll-off frequency of  $y$  is voltage-dependent due to the voltage dependence of  $\omega_g$ .

With the connectivity of Fig. A2, it is difficult to make high frequency roll off of both quantities as similar as the experimental data. For  $y$  to roll off at relatively high frequency,  $\omega_1$  has to be small and  $\omega_2$  has to be large because  $G_1$

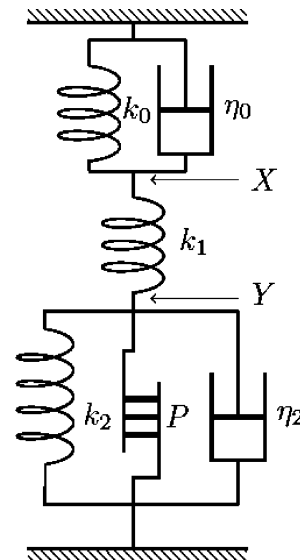


Figure A4. Schematic diagram of a cell with an alternative complex mechanical relaxation. The top dashpot  $\eta_1$  in Fig. A2 is replaced by a combination of a dashpot  $\eta_0$  and an elastic element  $k_0$ .

must be small as required by Eq. A30. This requirement makes  $x$  roll off at a frequency much lower than  $y$  does (Fig. A3).

### Modified complex mechanical relaxation

The model described above predicts a difference between  $x$  and  $y$  much larger than the experimentally observed frequency dependence. Let us add a spring across the upper dashpot (Fig. A4).

The set of equations that describe this configuration are

$$\left(\eta_0 \frac{d}{dt} + k_0\right)X = k_1(Y - X), \tag{A31}$$

$$F + \left(\eta_2 \frac{d}{dt} + k_2\right)Y = -k_1(Y - X). \tag{A32}$$

If force  $F$  is driven at angular frequency  $\omega$  with amplitude  $f$ , the equation is transformed into

$$(i\omega\eta_0 + k_0)x = k_1(y - x), \tag{A33}$$

$$f + (i\omega\eta_2 + k_2)y = -k_1(y - x), \tag{A34}$$

where variables in the lower case  $x$  and  $y$  are the complex amplitude of frequency  $\omega$ .

Eqs. A33 and A34 can be rewritten as

$$x = \frac{k_1}{k_0 + k_1 + i\omega\eta_0} \cdot y, \tag{A35}$$

$$f = k_1x - (k_1 + k_2 + i\omega\eta_2)y. \tag{A36}$$

In the manner similar to Eqs. A27 and A28 in the previous case, these equations can be expressed as

$$y = f/G_2(\omega), \tag{A37}$$

$$G_2(\omega) = \frac{k_1}{k_0 + k_1 + i\omega\eta_0} - (k_1 + k_2 + i\omega\eta_2), \tag{A38}$$

which corresponds to  $G_1(\omega)$  in the previous case.

Since force generation is associated with spring  $k_2$  in the manner similar to the previous case, we obtain

$$[G_2(\omega) + k_2]y = \frac{\beta a q k_2 \bar{P}_\pm}{1 + i\omega/\omega_g} \cdot v, \quad (\text{A39})$$

and  $x$  is obtained with Eq. A35.

If the cell contains  $N$  motile units,  $a$  should be replaced by  $aN$ . For numerical analysis, the number of parameters can be reduced by introducing the ratios  $k_{02} (= k_0/k_2)$ ,  $k_{12} (= k_1/k_2)$ ,  $\omega_0 (= k_2/\eta_0)$ , and  $\omega_2 (= k_2/\eta_2)$  and  $x$  and  $y$  are expressed by

$$x = \frac{k_{12}}{k_{02} + k_{12} + i\omega/\omega_0} \cdot y, \quad (\text{A40})$$

$$y = \frac{\beta a q N \bar{P}_\pm}{1 + i\omega/\omega_g} \cdot \frac{1}{k_{12}^2 / (k_{01} + k_{12} + i\omega/\omega_0) - (k_{12} + i\omega/\omega_2)} \cdot v. \quad (\text{A41})$$

The corresponding equations (Eq. 10) in the main text are expressed with linear frequency  $f$  instead of angular frequency  $\omega$ . Because these equations depend only on frequency ratios, no extra factor appears.

## Acknowledgments

Richard W. Aldrich served as editor.

This research was supported by National Institute on Deafness and Other Communication Disorders, National Institutes of Health grants R01 DC000273, R01 DC016318, and R01 DC008130 to J. Santos-Sacchi.

The authors declare no competing financial interests.

Author contributions: J. Santos-Sacchi conceived and performed experiments and wrote paper. W. Tan performed experiments. K.H. Iwasa did the modeling for the Appendix and wrote the Appendix and parts of the paper concerning this modeling.

Submitted: 23 October 2018

Revised: 24 August 2019

Accepted: 30 September 2019

## References

- Ashmore, J.F. 1987. A fast motile response in guinea-pig outer hair cells: the cellular basis of the cochlear amplifier. *J. Physiol.* 388:323–347. <https://doi.org/10.1113/jphysiol.1987.sp016617>
- Ashmore, J.F. 1990. Forward and reverse transduction in the mammalian cochlea. *Neurosci. Res. Suppl.* 12:S39–S50. [https://doi.org/10.1016/0921-8696\(90\)90007-P](https://doi.org/10.1016/0921-8696(90)90007-P)
- Ashmore, J. 2008. Cochlear outer hair cell motility. *Physiol. Rev.* 88:173–210. <https://doi.org/10.1152/physrev.00044.2006>
- Ashmore, J., P. Avan, W.E. Brownell, P. Dallos, K. Dierkes, R. Fettiplace, K. Grosh, C.M. Hackney, A.J. Hudspeth, F. Jülicher, et al. 2010. The remarkable cochlear amplifier. *Hear. Res.* 266:1–17. <https://doi.org/10.1016/j.heares.2010.05.001>
- Bai, J.P., A. Surguchev, Y. Ogando, L. Song, S. Bian, J. Santos-Sacchi, and D. Navaratnam. 2010. Prestin surface expression and activity are augmented by interaction with MAP1S, a microtubule-associated protein. *J. Biol. Chem.* 285:20834–20843. <https://doi.org/10.1074/jbc.M110.117853>
- Dallos, P., and B.N. Evans. 1995. High-frequency motility of outer hair cells and the cochlear amplifier. *Science.* 267(5206):2006–2009. <https://doi.org/10.1126/science.7701325>

- Dallos, P., X. Wu, M.A. Cheatham, J. Gao, J. Zheng, C.T. Anderson, S. Jia, X. Wang, W.H. Cheng, S. Sengupta, et al. 2008. Prestin-based outer hair cell motility is necessary for mammalian cochlear amplification. *Neuron.* 58:333–339. <https://doi.org/10.1016/j.neuron.2008.02.028>
- Dong, X.X., and K.H. Iwasa. 2004. Tension sensitivity of prestin: comparison with the membrane motor in outer hair cells. *Biophys. J.* 86:1201–1208. [https://doi.org/10.1016/S0006-3495\(04\)74194-6](https://doi.org/10.1016/S0006-3495(04)74194-6)
- Dong, W., and E.S. Olson. 2013. Detection of cochlear amplification and its activation. *Biophys. J.* 105:1067–1078. <https://doi.org/10.1016/j.bpj.2013.06.049>
- Duret, G., F.A. Pereira, and R.M. Raphael. 2017. Difflunilal inhibits prestin by chloride-dependent mechanism. *PLoS One.* 12:e0183046. <https://doi.org/10.1371/journal.pone.0183046>
- Frank, G., W. Hemmert, and A.W. Gummer. 1999. Limiting dynamics of high-frequency electromechanical transduction of outer hair cells. *Proc. Natl. Acad. Sci. USA.* 96:4420–4425. <https://doi.org/10.1073/pnas.96.8.4420>
- Gale, J.E., and J.F. Ashmore. 1994. Charge displacement induced by rapid stretch in the basolateral membrane of the guinea-pig outer hair cell. *Proc. Biol. Sci.* 255:243–249. <https://doi.org/10.1098/rspb.1994.0035>
- Gale, J.E., and J.F. Ashmore. 1997a. An intrinsic frequency limit to the cochlear amplifier. *Nature.* 389:63–66. <https://doi.org/10.1038/37968>
- Gale, J.E., and J.F. Ashmore. 1997b. The outer hair cell motor in membrane patches. *Pflügers Arch.* 434:267–271. <https://doi.org/10.1007/s004240050395>
- Gillis, K.D. 1995. Techniques for Membrane Capacitance Measurements. In *Single Channel Recording.* B. Sakmann, and E. Neher, editors. Plenum Press, New York. 155–198. [https://doi.org/10.1007/978-1-4419-1229-9\\_7](https://doi.org/10.1007/978-1-4419-1229-9_7)
- Hallworth, R.. 2007. Absence of voltage-dependent compliance in high-frequency cochlear outer hair cells. *J. Assoc. Res. Otolaryngol.* 8(4): 464–473. <https://doi.org/10.1007/s10162-007-0097-4>
- He, D.Z., and P. Dallos. 1999. Somatic stiffness of cochlear outer hair cells is voltage-dependent. *Proc. Natl. Acad. Sci. U.S.A.* 96(14):8223–8228. <https://doi.org/10.1073/pnas.96.14.8223>
- He, D.Z., and P. Dallos. 2000. Properties of voltage-dependent somatic stiffness of cochlear outer hair cells. *J. Assoc. Res. Otolaryngol.* 1(1):64–81. <https://doi.org/10.1007/s101620010006>
- He, W., D. Kemp, and T. Ren. 2018. Timing of the reticular lamina and basilar membrane vibration in living gerbil cochlea. *eLife.* 7:e37625. <https://doi.org/10.7554/eLife.37625>
- Homma, K., C. Duan, J. Zheng, M.A. Cheatham, and P. Dallos. 2013. The V499G/Y501H mutation impairs fast motor kinetics of prestin and has significance for defining functional independence of individual prestin subunits. *J. Biol. Chem.* 288:2452–2463. <https://doi.org/10.1074/jbc.M112.411579>
- Huang, G., and J. Santos-Sacchi. 1993. Mapping the distribution of the outer hair cell motility voltage sensor by electrical amputation. *Biophys. J.* 65: 2228–2236. [https://doi.org/10.1016/S0006-3495\(93\)81248-7](https://doi.org/10.1016/S0006-3495(93)81248-7)
- Iwasa, K.H. 1993. Effect of stress on the membrane capacitance of the auditory outer hair cell. *Biophys. J.* 65:492–498. [https://doi.org/10.1016/S0006-3495\(93\)81053-1](https://doi.org/10.1016/S0006-3495(93)81053-1)
- Iwasa, K.H. 1997. Current noise spectrum and capacitance due to the membrane motor of the outer hair cell: theory. *Biophys. J.* 73:2965–2971. [https://doi.org/10.1016/S0006-3495\(97\)78325-5](https://doi.org/10.1016/S0006-3495(97)78325-5)
- Iwasa, K.H.. 2000. Effect of membrane motor on the axial stiffness of the cochlear outer hair cell. *J. Acoust. Soc. Am.* 107(5 Pt 1):2764–2766. <https://doi.org/10.1121/1.428663>
- Iwasa, K.H. 2016. Energy Output from a Single Outer Hair Cell. *Biophys. J.* 111: 2500–2511. <https://doi.org/10.1016/j.bpj.2016.10.021>
- Iwasa, K.H., and B. Kachar. 1989. Fast in vitro movement of outer hair cells in an external electric field: effect of digitonin, a membrane permeabilizing agent. *Hear. Res.* 40:247–254. [https://doi.org/10.1016/0378-5955\(89\)90165-2](https://doi.org/10.1016/0378-5955(89)90165-2)
- Izumi, C., J.E. Bird, and K.H. Iwasa. 2011. Membrane thickness sensitivity of prestin orthologs: the evolution of a piezoelectric protein. *Biophys. J.* 100:2614–2622. <https://doi.org/10.1016/j.bpj.2011.04.032>
- Johnson, S.L., M. Beurg, W. Marcotti, and R. Fettiplace. 2011. Prestin-driven cochlear amplification is not limited by the outer hair cell membrane time constant. *Neuron.* 70:1143–1154. <https://doi.org/10.1016/j.neuron.2011.04.024>
- Kachar, B., W.E. Brownell, R. Altschuler, and J. Fex. 1986. Electrokinetic shape changes of cochlear outer hair cells. *Nature.* 322(6077):365–368.
- Kitani, R., S. Kakehata, and F. Kalinec. 2011. Motile responses of cochlear outer hair cells stimulated with an alternating electrical field. *Hear. Res.* 280(1–2):209–218. <https://doi.org/10.1016/j.heares.2011.05.013>



- Kolb, H.A., and P. Luger. 1978. Spectral analysis of current noise generated by carrier-mediated ion transport. *J. Membr. Biol.* 41:167–187. <https://doi.org/10.1007/BF01972631>
- Meltzer, J., and J. Santos-Sacchi. 2001. Temperature dependence of nonlinear capacitance in human embryonic kidney cells transfected with prestin, the outer hair cell motor protein. *Neurosci. Lett.* 313:141–144. [https://doi.org/10.1016/S0304-3940\(01\)02266-2](https://doi.org/10.1016/S0304-3940(01)02266-2)
- Oliver, D., D.Z. He, N. Klocker, J. Ludwig, U. Schulte, S. Waldegger, J.P. Ruppersberg, P. Dallos, and B. Fakler. 2001. Intracellular anions as the voltage sensor of prestin, the outer hair cell motor protein. *Science*. 292: 2340–2343. <https://doi.org/10.1126/science.1060939>
- Pusch, M., and E. Neher. 1988. Rates of diffusional exchange between small cells and a measuring patch pipette. *Pflügers Arch.* 411:204–211. <https://doi.org/10.1007/BF00582316>
- Ren, T., W. He, and D. Kemp. 2016. Reticular lamina and basilar membrane vibrations in living mouse cochleae. *Proc. Natl. Acad. Sci. USA.* 113: 9910–9915. <https://doi.org/10.1073/pnas.1607428113>
- Reuter, G., A.H. Gitter, U. Thurm, and H.P. Zenner. 1992. High frequency radial movements of the reticular lamina induced by outer hair cell motility. *Hear. Res.* 60(2):236–246. [https://doi.org/10.1016/0378-5955\(92\)90025-i](https://doi.org/10.1016/0378-5955(92)90025-i)
- Santos-Sacchi, J. 1989. Asymmetry in voltage-dependent movements of isolated outer hair cells from the organ of Corti. *J. Neurosci.* 9:2954–2962. <https://doi.org/10.1523/JNEUROSCI.09-08-02954.1989>
- Santos-Sacchi, J. 1991. Reversible inhibition of voltage-dependent outer hair cell motility and capacitance. *J. Neurosci.* 11:3096–3110. <https://doi.org/10.1523/JNEUROSCI.11-10-03096.1991>
- Santos-Sacchi, J.. 1992. On the frequency limit and phase of outer hair cell motility: effects of the membrane filter. *J. Neurosci.* 12(5):1906–1916. .
- Santos-Sacchi, J. 2004. Determination of cell capacitance using the exact empirical solution of dY/dCm and its phase angle. *Biophys. J.* 87:714–727. <https://doi.org/10.1529/biophysj.103.033993>
- Santos-Sacchi, J. 2018. High frequency measures of OHC nonlinear capacitance (NLC) and their significance: Why measures stray away from predictions. AIP Conference Proceedings 1965:060004–060001–060004–060005.
- Santos-Sacchi, J. 2019. The speed limit of outer hair cell electromechanical activity. *HNO.* 67:159–164. <https://doi.org/10.1007/s00106-019-0615-9>
- Santos-Sacchi, J., and J.P. Dilger. 1988. Whole cell currents and mechanical responses of isolated outer hair cells. *Hear. Res.* 35:143–150. [https://doi.org/10.1016/0378-5955\(88\)90113-X](https://doi.org/10.1016/0378-5955(88)90113-X)
- Santos-Sacchi, J., and L. Song. 2014a. Chloride and salicylate influence prestin-dependent specific membrane capacitance: support for the area motor model. *J. Biol. Chem.* 289:10823–10830. <https://doi.org/10.1074/jbc.M114.549329>
- Santos-Sacchi, J., and L. Song. 2014b. Chloride-driven electromechanical phase lags at acoustic frequencies are generated by SLC26a5, the outer hair cell motor protein. *Biophys. J.* 107:126–133. <https://doi.org/10.1016/j.bpj.2014.05.018>
- Santos-Sacchi, J., and L. Song. 2016. Chloride anions regulate kinetics but not voltage-sensor Qmax of the solute carrier SLC26a5. *Biophys. J.* 110: 2551–2561. <https://doi.org/10.1016/j.bpj.2016.05.002>
- Santos-Sacchi, J., and W. Tan. 2018. The Frequency Response of Outer Hair Cell Voltage-Dependent Motility Is Limited by Kinetics of Prestin. *J. Neurosci.* 38:5495–5506. <https://doi.org/10.1523/JNEUROSCI.0425-18.2018>
- Santos-Sacchi, J., S. Takehata, and S. Takahashi. 1998. Effects of membrane potential on the voltage dependence of motility-related charge in outer hair cells of the guinea-pig. *J. Physiol.* 510:225–235. <https://doi.org/10.1111/j.1469-7793.1998.225bz.x>
- Santos-Sacchi, J., W. Shen, J. Zheng, and P. Dallos. 2001. Effects of membrane potential and tension on prestin, the outer hair cell lateral membrane motor protein. *J. Physiol.* 531:661–666. <https://doi.org/10.1111/j.1469-7793.2001.0661h.x>
- Santos-Sacchi, J., D. Navaratnam, R. Raphael, and D. Oliver. 2017. The Cochlea Chapter 5: Prestin - molecular mechanisms underlying outer hair cell electromotility. In *Springer Handbook Of Auditory Research*. Springer, New York.
- Schnee, M.E., J. Santos-Sacchi, M. Castellano-Muñoz, J.H. Kong, and A.J. Ricci. 2011a. Calcium-dependent synaptic vesicle trafficking underlies indefatigable release at the hair cell afferent fiber synapse. *Neuron.* 70: 326–338. <https://doi.org/10.1016/j.neuron.2011.01.031>
- Schnee, M.E., M. Castellano-Muñoz, J.H. Kong, J. Santos-Sacchi, and A.J. Ricci. 2011b. Tracking vesicle fusion from hair cell ribbon synapses using a high frequency, dual sine wave stimulus paradigm. *Commun. Integr. Biol.* 4:785–787. <https://doi.org/10.4161/cib.17822>
- Song, L., and J. Santos-Sacchi. 2013. Disparities in voltage-sensor charge and electromotility imply slow chloride-driven state transitions in the solute carrier SLC26a5. *Proc. Natl. Acad. Sci. USA.* 110:3883–3888. <https://doi.org/10.1073/pnas.1218341110>
- Vavakou, A., N.P. Cooper, and M. van der Heijden. 2019. The frequency limit of outer hair cell motility measured in vivo. *Elife.* 8. <https://doi.org/10.7554/eLife.47667>
- Zheng, J., W. Shen, D.Z. He, K.B. Long, L.D. Madison, and P. Dallos. 2000. Prestin is the motor protein of cochlear outer hair cells. *Nature.* 405: 149–155. <https://doi.org/10.1038/35012009>